Aalto University
School of Electrical
Engineering

Master's programme in ICT Innovation

A Multibody Approach for Modelling of Rope Dynamics

Matteo Mastrogiuseppe

Master's Thesis
2023

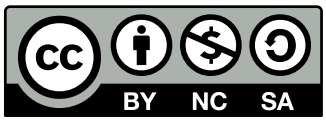

Aalto University
School of Electrical
Engineering

Author Matteo Mastrogiuseppe

Title A Multibody Approach for Modelling of Rope Dynamics

Degree programme ICT Innovation

Major Autonomous Systems

Supervisor Prof. Quan Zhou

Advisor Sunayna Singh (MSc.)

Collaborative partner German Aerospace Center (DLR)

Date 14 September 2023 **Number of pages** 78+4 **Language** English

Abstract

The 'In-Air Capturing' method is a novel approach for the recovery of space launch vehicles, where an airplane catches a winged rocket stage in mid-air and tows it back to the launch site. Since no descent propulsion system is required, the Reusable Launch Vehicle is less expensive than traditional techniques. During the In-Air Capturing maneuver, a capturing device attached to a rope is released from the towing aircraft. While the two vehicles are in close proximity to one another, this device autonomously connects the rocket to the airplane. For a successful capture, this device must move with agility and accuracy, despite the vibrations from the long rope (up to 300 m) and external disturbances. Therefore, modeling the flexible dynamics of the rope is essential to have a realistic understanding of the device's maneuverability and the viability of the concept.

Such highly flexible systems with significant deformation are difficult to model and manage and require intense computation. Driven by these requirements, we propose and examine a new multibody approach that provides a balance between accuracy and computation time. The rope can be modelled as a discretized chain of rigid bodies connected at the joints. The model also includes forces originating from the capturing device, the drag of the rope and the effect of the aircraft wake. To deal with rope features such as the bending stiffness and elongation, we adopt simplifying assumptions, with the goal to reduce the overall computational effort. Such assumptions are expected to hold, in the scenario of interest. To select rope fitting properties like material, diameter and length, we use the requirements imposed by the In-Air-Capturing application.

Results show that the model provides a valid description of the underlying physics. Simulations of the In-Air-Capturing procedure demonstrate the capacity of the rope to sustain the loads associated with towing the rocket, while also allowing for large maneuverability for the capturing device.

Overall, this thesis presents an accurate yet computationally efficient modelling approach for rope dynamics, with a special focus on the implications on the In-Air Capturing maneuver. This framework is also applicable to a wide range of dynamic simulations involving long, slender, flexible structures (such as air-to-air refueling).

Keywords Reusable Launch Vehicles, Multibody Simulation, Numerical Integration

Preface

This work was conducted during my staying at DLR's SART Department, in Bremen. I would like to express my gratitude to all the colleagues I was lucky to meet and work with. Special thanks to Sunayna Singh, for being such a great and kind advisor. Thank you for your patience when introducing me to this project, and for your unwavering support throughout. A particular mention also to Tommaso, for always being helpful and a valid GeoGuessr opponent.

I want to thank my Aalto supervisor Quan Zhou, for the valuable comments and for the availability. I would also like to acknowledge Professors Biral and Bortoluzzi from University of Trento, whose teaching greatly inspired the methodology used in this research.

My heartfelt gratitude goes out to my friends from Trento and Aalto University for turning my Master's studies into an unforgettable international experience. Special note to the amazing people of the *AUSgang*. I am much obliged to EIT Digital, for allowing such a wonderful opportunity and experience.

Finally, I'd love to thank my family for the endless, priceless support. Truly a "Poca gente a Chieti" moment.

Otaniemi, 14 September 2023

Matteo Mastrogiuseppe

Contents

Symbols and abbreviations

Symbol	Description	Unit Measure
L_{tot}	Total length of the rope	m
m_{tot}	Total mass of the rope	kg
n	Number of rope segments	-
L	Length of a single rope segment	m
m	Mass of a single rope segment	kg
ϕ_i	Azimuth angle for rope element	rad
ψ_i	Side-slip angle for rope element	rad
$\dot{\phi}_i, \dot{\psi}_i$	Angular velocities of the rope element	$\mathrm{rad\,s^{-1}}$
$\boldsymbol{r}_p$	Cartesian position of a point	m
x, y, z	Cartesian position components of a point	m
v_x, v_y, v_z	Cartesian velocity coordinates of a point	$\mathrm{m\ s^{-1}}$
a_x, a_y, a_z	Cartesian coordinates of point acceleration	$\mathrm{m\ s^{-2}}$
$\mathcal{L}$	Lagrangian of the system	J
T	Kinetic energy of the system	J
V	Potential energy of the system	J
I	Moment of inertia of the rope element	$\mathrm{kg\ m^2}$
g	Gravitational acceleration constant	$\mathrm{m\,s^{-2}}$
q	Generalized coordinate for the system	-
Q	Generalized force for the system	-
$\boldsymbol{F}$	Force expressed in Cartesian coordinates	N
K_t	Rope bending stiffness coefficient	$\mathrm{N\,m^2}$
γ	Generic curve as a parametric function	m
R	Radius of curvature	m
θ_i	Relative rotation generalized coordinate	rad
M	Bending moment	N m
δW_j	Virtual work associated with force j	J
c	Angular damping coefficient	$\mathrm{N\,m\,s\,kg^{-1}}$
$\boldsymbol{T}$	Coordinate transformation matrix	-
F_D, C_D	Drag force and relative coefficient	-
F_L, C_L	Lift force and relative coefficient	-
ρ	Fluid mass density	$\mathrm{m^3\,kg^{-1}}$
d	Rope diameter	m
A	Body reference area	$\mathrm{m^2}$
α_{tot}	Total angle of attack	rad
s	Rope elongation variable	m
k_a	Axial spring elastic coefficient	N m
c_k	Axial spring damper coefficient	$\mathrm{N\,s\,(m\,kg)^{-1}}$
E	Young's modulus	GPa
T_{max}	Rope breaking strength	N
U	Mechanical energy of the system	J

$\boldsymbol{M}$	System's mass matrix	-
$\boldsymbol{f}$	System's right-hand side	-
k	Total number of variables of the system	-
$\hat{\boldsymbol{M}}$	Mass matrix (first-order system)	-
$\hat{\boldsymbol{f}}$	Right-hand side (first-order system)	-
$\boldsymbol{X}$	System state variables (first-order)	-
h	Integration time step	s

Operators

$\frac{\mathrm{d}}{\mathrm{d}t}$	derivative with respect to variable t
$\frac{\partial}{\partial t}$	partial derivative with respect to variable t
$\sum_i$	sum over index i
$\int_A$	integral over domain A
$\mathbf{A} \cdot \mathbf{B}$	dot product of vectors **A** and **B**

Abbreviations

ACCD	Aerodynamically Controlled Capturing Device
DLR	German Aerospace Center
IAC	In-Air Capturing
MBS	Multibody System
ODE	Ordinary Differential Equation
RLV	Reusable Launch Vehicles
TA	Towing Aircraft

1 Introduction

1.1 The 'In-Air Capturing' Maneuver

In the recent years, the evolution of Reusable Launch Vehicles (RLV) has made it possible to achieve higher launch frequencies while managing the costs [1][2]. The solutions that have been proposed and developed can be divided in two main categories, based on how the launch vehicle achieves landing:

- Vertical Take-off Horizontal Landing. This was the first implemented approach, with the Space Shuttle [3] being the first ever partially reusable spacecraft system.
- Vertical Take-off Vertical Landing. This procedure is used in the Falcon 9 launch vehicle, manufactured by SpaceX, which has become the de facto state of the art in space launching systems. The under development Ariane Next, from the European Space Agency and manufactured by ArianeGroup, aims at using a similar approach [4].

Both approaches have proven to be successful, with vertical landing being prevalent nowadays. However, they show room for cost reduction. Vertically landing vehicles require a significant amount of fuel to successfully land stages in appropriate sites. On the contrary, in horizontal landing configurations, the adoption of winged stages requires an extra propulsion system to land horizontally. In both cases the stage mass is increased, reducing the room for payload.

A new and innovative recovery method is the In-Air Capturing (IAC) maneuver, a patented approach by German Aerospace Center (DLR) [5]. This concept involves winged rocket stages being captured while mid-air and towed back to the launch site using an external aircraft. It shows potential for considerable cost reduction as it allows the vehicle to land without using an additional propulsion system during descent.

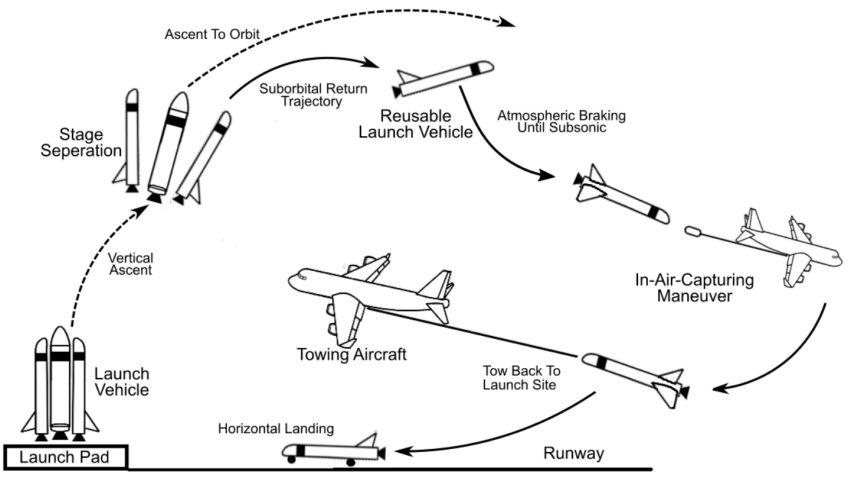

Figure 1.1: Scheme of the IAC mission cycle (Source: [2]).

Figure 1.1 depicts the complete and standard operational sequence of the IAC [2] [6]. The mission begins with a vertical lift-off from the launch pad. Following Main Engine Cut Off, the winged initial stage disconnects from the launch vehicle, while the second stage progresses into orbit. The first stage then proceeds with a ballistic re-entry, making use of atmospheric resistance to decrease its velocity to subsonic levels. Meanwhile, a Towing Aircraft (TA) remains stationed at an altitude of approximately 10 km until the RLV approaches. Subsequently, within the altitude range of 2 km to 8 km, the TA maneuvers to meet the RLV, establishing a synchronized gliding formation. During this intricate procedure, an Aerodynamically Controlled Capturing Device (ACCD) attached to a rope is released from the TA. This mechanism autonomously navigates towards the RLV, ensuring a secure connection between the two entities. Ultimately, the RLV is guided back to an airstrip, to perform a horizontal landing.

The IAC maneuver is a highly complex engineering mission, which requires extreme precision and coordination. It is crucial to validate this approach and demonstrate its feasibility, in all the phases of the mission. This research focuses on the capturing maneuver, most specifically in the simulation of the dynamics of the flexible rope found in the capturing system, with the ACCD attached to its end.

To better understand the challenges arising from the capturing task, we can divide it into sub-phases, as shown in Figure 1.2:

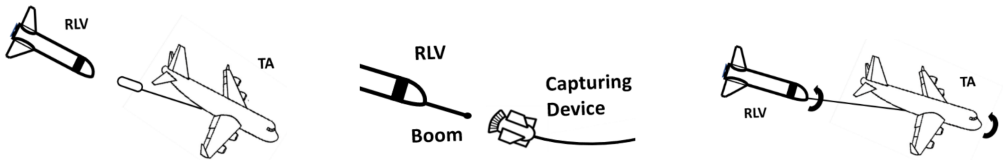

(a) Formation Flight **(b)** Capture Phase **(c)** Pull-up Manoeuvre

Figure 1.2: Sub-phases of the capturing process (Source: [7]).

- *Phase 1: Formation Flight*
  The first phase consists in the TA approaching the RLV to begin the capturing process. With its engines off, the aircraft glides from the cruise condition, and joins the RLV in a parallel descending configuration. The two vehicles shall maintain comparable velocities and orientation, while being separated by a safety distance (between 150m and 350m). The formation configuration must kept for a sufficient amount of time, to ensure that the following phase is successfully accomplished.

- *Phase 2: Capture Phase*
  The capture phase is conducted when the two vehicles have achieved formation. During this maneuver, the ACCD, attached to a rope, is released from the TA. This device is provided with controllable flaps, so that it can guide its way to the RLV and guarantee the connection between the two bodies. This phase is especially critical, because a number of aspects must be considered to secure a success mating. The aerodynamics of the ACCD and the rope must be studied in detail, possibly checking the effect of the wake generated by the

TA. Furthermore, the rope dynamics might have a major impact on the stability of the system, so the sensitivity to its properties requires investigation. The response of the system to generic control deflections to the ACCD flaps must also be studied.

- *Phase 3: Pull-up Manoeuvre*
  Once the two vehicles are connected through the capturing system, the aircraft effectively acts like an external propulsion system to the RLV. Turning on the the TA engines, it is possible to execute a pull-up manoeuvre to transition to an ascending flight. In this phase the rope is under the most stress, because of the aircraft thrust and forces coming from the RLV. After this, the mission proceeds with the later steps, until the horizontal landing.

1.2 Problem Statement

An essential aspect of IAC simulations is the precise modelling of the capturing system, comprising a long rope and a capturing device attached to its end. Establishing a connection between the ACCD and the RLV is a highly complex task. The ACCD shall be able to autonomously navigate its way to the RLV, successfuly mating the two vehicles. To achieve this, the ACCD is equipped with control surfaces, notably flaps situated at the bottom of the fins. Given that the capturing device is positioned at the end of the flexible rope, its position and orientation are extremely sensitive to vibrations, perturbations, and general rope displacements. The control strategies are designed to guide the ACCD towards the RLV's position, serving as the primary objective of the capturing phase. Consequently, to meet the stringent requirements of the application, the physical modelling of the rope must provide accurate outcomes.

Under steady-state conditions of the capturing system, the rope is likely to assume a predominantly straight configuration due to the heavy loads involved in the application. From a modelling standpoint, it may not be necessary to describe configurations with large oscillations or flexed rope configurations. Therefore, past rope models have utilized simple beam-like elements to simplify the representation. However, this work endeavors to minimize such simplifying assumptions.

Modelling and control of such highly flexible systems, with large deformation and displacement, is both challenging and computationally intensive. Conventional simulation frameworks are ill-suited for this task, as it involves a highly nonlinear body dynamics problem with ropes characterized by nearly infinite degrees of freedom. However, considering the size and complexity of the general environment (including the Towing Aircraft, Reusable Launch Vehicle, and atmosphere models), it is imperative to keep the computational effort for rope modelling within reasonable limits. One of the primary focus of this work is to explore a reasonable accuracy-computation trade-off. In multibody dynamics simulation, this often deals with the choice of formulation or modelling approach. As it will be later discussed, the modelling of rope dynamics inevitably requires discretization of the rope into sub-elements, regardless of the chosen formulation. Adjusting the discretization hyperparameter appropriately becomes a straightforward method to reduce computational effort.

The accuracy-computation trade-off can also be investigated in terms of the integration of the Ordinary Differential Equation (ODE). The simulation aims to utilize integration step-sizes as large as possible to minimize the frequency of calls to the function computing the equations of motion. However, using a large step-size may compromise accuracy and potentially lead to stability issues. The larger scale simulation of the IAC maneuver operates with a time step of 10^{-2} s, due to the implementation of control strategies. Consequently, the rope model must remain stable for this step size. Additionally, mechanical systems often lead to a "stiff" set of equations of motion, susceptible to instability unless the time step is very small. In this context, identifying the right numerical algorithm that avoids instability issues while optimizing computation time is crucial.

1.3 Model requirements

The problem statement translates into a set of requirements for the model.

- The model shall provide an accurate and realistic description of the rope dynamics. The material properties of the rope must be incorporated into the model, such as mass, length, Young modulus. In order to represent the rope's large displacement and deformation, a suitable modelling formulation must be used.

- The modelling approach should be computationally efficient, allowing to run the simulation in a reasonable time frame. The software implementation of the model shall eventually adopt approaches to speed-up the computation such as parallel processing computing.

- From an implementation perspective, the developed model shall be flexible enough to incorporate all kinds of forces which have an impact on the system's dynamics. External forces and disturbances, such as the wake generated by the aircraft and the rope lift and drag, must be easy to model and be included in the system. Not only, the rope is also subject to inertia effects, generated by accelerations in the TA motion. The two systems are constrained by a fixed joint, so turbulence or variations in the motors' thrust will have a direct impact on the rope dynamics.

- The ODE solver of choice must maintain simulation stability with the predetermined time step, while guaranteeing computational efficiency. This necessitates an exploration of explicit and implicit methods, along with a thorough consideration of their key properties and the effect of the order of integrator.

In the following chapter, the suitability of the possible modelling approaches will be evaluated with respect to these requirements.

1.4 Aim of the Research

The objective of the present work is to identify an appropriate approach for the modelling of the rope dynamics in the context of the IAC maneuver. The formulation aims at best solving the list of requirements coming from the field of application, while also being flexible enough to be expanded in other contexts. Initially, various approaches documented in the literature will be investigated and evaluated. The most promising formulation is decided based on its potential to match the set of requirements. Based on this, a new Multibody System (MBS) is proposed, aimed at extending the existing model through the incorporation of new dynamic features.

The original contributions need experimental data to be fully validated. While this is left for future research, this thesis aims to demonstrate the solidity of the chosen approach and to highlight both its advantages and drawbacks. Subsequently, the model is employed within the context of IAC simulations to identify appropriate rope specifications that align with the mission's requirements.

Based on this, a list of research questions is derived:

- Does the model provide a sufficiently accurate representation of the physics governing the rope dynamics? Can it effectively describe the oscillations commonly observed in slender bodies?
- What are the appropriate rope material and specifications for the IAC mission?
- Is the capturing system stable in the reference configuration? Does the wake of the aircraft affect the maneuverability of the system?
- Does the final set of ODEs manifest numerical problems during the integration? Is it sensitive to the type of ODE solver used and the choice of the integration step size?
- Is it possible to achieve a reasonable trade-off between accuracy and computation time?

Potential answers to these questions will be discussed in the 'Conclusion' section, while supporting arguments will be shown in the 'Results' section.

1.5 Thesis Overview

The structure of this work follows a systematic workflow.

Chapter 2 presents an overview of existing models and techniques available in the literature, along with a critical examination of their alignment with the specified requirements. The most appropriate approach is then selected, and the rationale behind its adoption is elaborated.

Chapter 3 provides a comprehensive examination of the proposed MBS, including a detailed derivation of the equations of motion using the Lagrange approach. Methods to incorporate the rope features, such as stiffness and elongation are presented. The

final integration scheme is presented, accompanied by strategies to ensure efficient implementation of the model in software.

Finally, Chapter 4 presents the simulation results. Issues concerning the validation of the proposed model are discussed. A verification of the model is performed by analyzing the energy balance in different test cases. Following, the results of the larger scale IAC simulation are shown. A sensitivity analysis of the rope parameters is presented, leading to the proposal of appropriate values for the rope specifications. These results are thoroughly discussed in terms of their implications on the feasibility of the IAC mission.

Based on these results, conclusions are drawn in Chapter 5. Limitation of the work and drawbacks of the approach are presented. Moreover, the chapter offers valuable recommendations to enhance the model and suggests directions for further research and development.

2 Literature Review

2.1 Mission Heritage

The dynamics of flexible ropes have been extensively researched due to their critical role in various industries and domains. Accurate modelling of rope physics is crucial for the development and optimization of many engineering systems. Hereafter the most prominent and correlated fields of application are listed.

- **Aerial Cabled-Towed Systems**: Aerial cabled-towed systems employ flexible ropes to provide mechanical support and guidance to airborne objects. Systems typically consist of a towing aircraft that pulls the airborne object using a flexible cable. The loads to be pulled can vary a lot depending on the application. They range from simple parafoils to gliders or unmanned aerial vehicles (UAVs). This kind of system is often implemented in defence applications. An example is the ALE-50 towed decoy system, which finds use in many fighter jets such as the U.S. Navy F Series. It is a countermeasure electronic device, which is deployed and towed behind the aircraft, as a way to lure enemy missiles away from the original target. Some other recent applications have seen much interest, like the use of a swarm of UAVs to lift generic loads in transportation businesses [8]. The dynamics of the flexible rope play a crucial role in maintaining stability, controlling the trajectory, and managing different stresses during the flight. A number of investigations have been conducted to research the dynamics of such systems, considering factors such as rope elasticity, tension control, aerodynamic effects, and environmental conditions.

- **Aerial Refueling**: Aerial refueling operations involve the use of flexible hoses to transfer fuel during flight from a tanker aircraft to a receiver (Figure 2.1) [9]. The dynamics of these ropes play a crucial role in maintaining stability, control, and safety during the refueling process [10].

  The system configuration is very similar to the IAC setup. Two subsystems, separated at the beginning, are required to couple in mid-air to achieve the primary goal of the mission, being refueling or towing. Therefore, it is reasonable to consider the hose modelling approaches as a valid option, or at least as a starting point. In fact, hoses are shorter and much stiffer than the ropes in question, so the dynamics of the two systems can be completely different. Moreover, the IAC procedure adds an extra layer of complexity, since the mating is supposed to be fully autonomous. On the contrary, aerial refueling procedures relies on the pilot's maneuvering.

Figure 2.1: Aerial Refueling system, tanker aircraft and receiver are in the coupled configuration (Source: [11]).

- **Space Tethers**: Space tethers are long, flexible structures deployed in space to facilitate various applications, including attitude control, propulsion, energy generation, and orbital maneuvering [12]. A space tether typically consists of a long, strong cable with one end attached to a spacecraft or a celestial body while the other end is left to extend freely in space (Figure 2.2). A number of studies have investigated the behavior and performance of space tethers, providing insights into their stability, deployment dynamics, and overall system design [13].

- **Space Elevators**: Space elevators are hypothetical structures that connect the Earth's surface to space, enabling the transportation of payloads along the tether using a combination of gravity and centrifugal force [14]. The concept involves a cable extending from the Earth's surface to a counterweight in space, with the gravitational force and centrifugal force maintaining tension in the cable. Space elevators offer a potential future method for efficient and cost-effective transportation to space. modelling the dynamics of space elevators involves considering various aspects, including tether material strength, elasticity, environmental effects, and orbital dynamics. Tether modelling plays a major role in demonstrating the feasibility of the concept. Approaches in the literature mainly make use of very simple models, given the enormous size of such system [15]. Tether is usually described as a 1D line with a straight configuration, and the estimate of the tension is obtained by integrating all contributes over the tether length. These models appear to be too simplistic for our application.

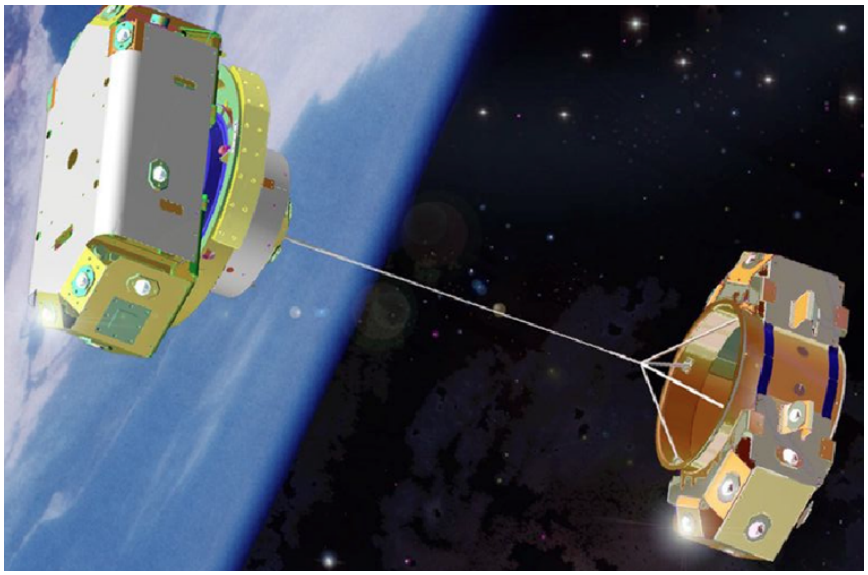

Figure 2.2: Rendering of a Space tether used in satellites applications (Source:[12]).

- **Cable Theory**: Cable theory focuses on the mathematical modelling of slender structures, taking into account their geometric and material properties. Theoretical frameworks and computational models have been developed to analyze the behaviour of cables subjected to various loading conditions, including static and dynamic loads [16]. Cable theory has found applications in several domains, including civil engineering, underwater systems, robotics, and bio-mechanics. Cable simplification mostly consists in neglecting torsional effects, so it can be used only in a limited number of scenarios. While cable-like elements are also used in civil and structural applications, these fields are not useful to our scope. In fact, approaches for structural cables don't aim at describing large deflections, but only the stresses coming from the static, reference configuration.

- **Computer Graphics**: modelling flexible ropes is a fundamental aspect of computer graphics, enabling realistic simulations of cloth, hair, ropes, and other deformable objects. Researchers have proposed various techniques to capture the dynamics of flexible ropes in computer-generated environments [17]. The most prominent approaches consists in mass-spring systems [18], position-based dynamics [19], and splines-based dynamics [20]. These models consider factors such as rope elasticity, collisions, self-interactions, and interactions with other objects. The main contribution of computer graphics in the simulation of slender, flexible bodies is the development of efficient algorithms. Visual realism and interactive behavior of virtual environments require limited computation effort in order to obtain real-time performances. Most of the times, this implies a limited description of the underlying physics, and the adoption of heuristic methods to accomplish a realistic simulation.

2.2 Modelling Approaches

Various methods have been suggested for modelling such a nonlinear system. Although the formulations can diverge significantly, the overarching strategy primarily revolves around subdividing the system into numerous sub-elements. Hereafter, we delve into the conventional techniques for simulating flexible bodies, aiming to identify the most suitable one for our specific application.

2.2.1 Floating Reference Frame

The Floating Reference Frame formulation has been the most widely used method in the simulation of flexible multibody systems. This formulation introduces a set of coordinates that characterize the body's deformation with respect to its coordinate system. This is in addition to the standard set of multibody variables used to describe the reference position and orientation of the chosen coordinate system. Therefore, a minor additional deformation is effectively superimposed.

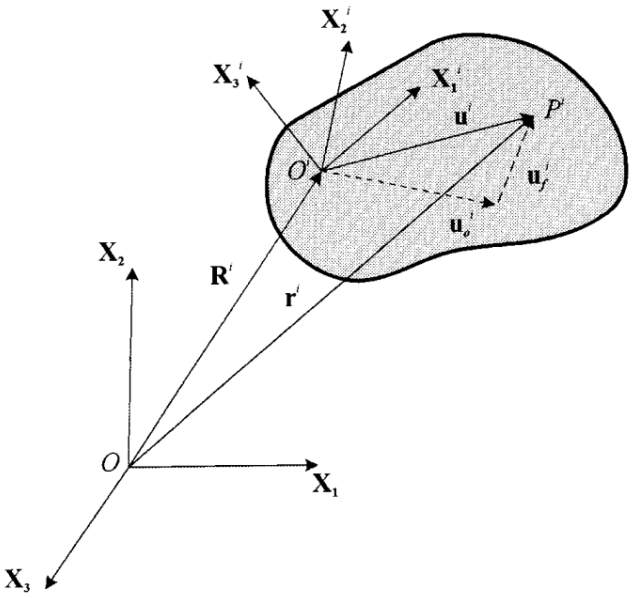

Figure 2.3: Description of the body kinematics, using the Floating Reference Frame. (Source: [21])

The position vector of any arbitrary point on the flexible body in the global frame can be expressed as follows [21]:

$$\boldsymbol{r} = \boldsymbol{R} + \boldsymbol{A}\left(\boldsymbol{u_0} + \boldsymbol{u}_f\right) \tag{2.1}$$

Figure 2.3 visualizes vectors of Eq. 2.1: $\boldsymbol{u_0}$ refers to the undeformed position, while $\boldsymbol{u}_f$ is the deformation variable. $\boldsymbol{A}$ is the transformation matrix, which defines the orientation of the body coordinate system with respect to the global frame.

By utilizing these sets of coordinates, it becomes possible to establish a local linear problem, thus enabling the application of modal reduction techniques [22].

In fact, one of the significant benefits of adopting the Floating Frame formulation is the availability of numerous modal order reduction alternatives, which allow a simplification of the system's representation. In some cases, this can even be achieved without sacrificing accuracy, through the implementation of techniques such as Proper Orthogonal Decomposition or other similar approaches. Additionally, the Floating Reference Frame facilitates the elimination of high-frequency vibration modes that have negligible influence on the solution.

On the other hand, the drawbacks associated with employing this formulation are considerable, considering the requirements. The mass matrix is highly non-linear and must be evaluated at every time-step. Furthermore, using the standard formulation, one must account for the presence of centrifugal, Coriolis, and generalized gravity forces in the equations of motion due to some variables being defined locally and not globally. The required computation is prone to be substantial. Ultimately, and of utmost importance, the floating frame of reference formulation has demonstrated to be most suitable for large reference displacement and small deformation analysis. This does not align well with the modelling of the rope dynamics, characterized by large deflection and deformation.

2.2.2 Approaches for Cable-like Bodies

Certain modelling methodologies, developed within the domain of cable-like structures, can be categorized as *continuous* models, as their primary emphasis lies in describing the central axis of linear objects [23]. Cable theory discusses the modelling of linear, slender entities, characterized by a significant disparity between the length of the structure and its cross-sectional dimensions. If one neglects the cross-section deformation, which is generated by torsional forces, then it might be reasonable to adopt such methods and formulations.
Hereafter, the most notable modelling formulations are analyzed:

- **Elastic rod model**: This model originates from the principles of continuum mechanics and conceptualizes flexible, elongated linear objects as elastic rods. This framework is backed by the foundational Kirchhoff theory [24], which describes bodies whose centerline is inextensible and whose cross sections remain plane and normal to the centerline. A more refined version, the Cosserat theory [25], was later proposed by the Cosserat brothers, enhancing the Kirchhoff theory by incorporating considerations for both axial extensional and sectional shear deformations. Although this approach has demonstrated its utility in analyzing the dynamic behavior of slender constructs, it does exhibit certain constraints. The elastic rod theory assumes modest deformations and strains, implying that the rod's geometry remains closely aligned with its original form. This assumption is inadequate for our particular application, which deals with large deformations and highly curved configurations. Furthermore, the theory generally presupposes an ideal elastic response, neglecting to account for damping or energy dissipation effects, which hold significant importance within the context of such simulations.

- **Dynamic spline model**: This method employs a spline curve to delineate the center axis of a flexible, cable-like linear object, while at the same time investing the spline curve with physical attributes like mass and deformation energy. This strategy ensures that the response to external forces and constraints eventually conforms to the principles of physics. A spline curve, characterized by its segmented polynomial nature in parametric configuration, is utilized. A curve composed of n control points (p_1, p_2, ..., p_n) can be expressed as [23]:

$$\boldsymbol{P}(u) = \sum_{i=1}^{n} b_i(u)\, \boldsymbol{p}_i$$

where $b_i(u)$ is the i_{th} spline basis function, of the control point p_i (as in Figure 2.4).

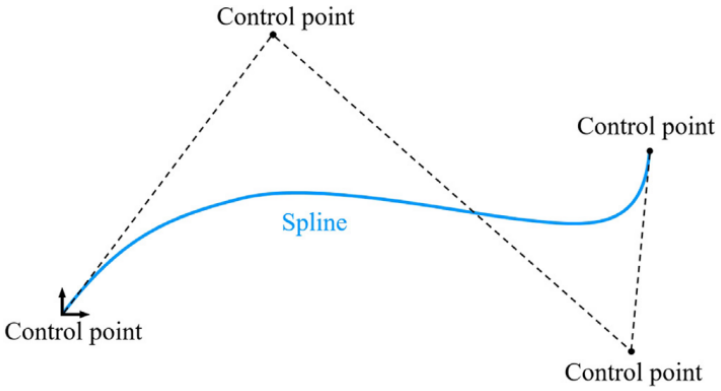

Figure 2.4: Spline curve for dynamic spline modelling.

The control points location are effectively the degrees of freedom of the spline, and have a major contribution to the shape of the spline along with the choice of the basis function. While this strategy might be efficient for 1D and 2D situations, especially when demanding fast and precise rendering, it proves to be less suitable for complex 3D multibody simulations. Moreover, spline models may not inherently encompass the material characteristics and physical responses of the actual bodies they represent.

2.2.3 ANCF Finite Element Formulation

The Absolute Nodal Coordinate Formulation (ANCF) is a recent finite element procedure, which has proven to be much effective in the description of large deformations and large rotations [26]. In this formulation, all nodal coordinates are defined in the inertial frame. No infinitesimal or finite rotations are used; instead, absolute slopes and displacements are used at the element nodal coordinate. These element coordinates are used with a global shape function that is capable of describing a complete set of rigid body modes. The globally referred position of a point can be thus written as:

$$\boldsymbol{r} = \boldsymbol{S}\boldsymbol{e} \tag{2.2}$$

where $\boldsymbol{S}$ is the global shape function and $\boldsymbol{e}$ is the vector of nodal coordinates. Figure 2.5 shows a simple, beam element which has two nodes, A and B, situated at its extremities.

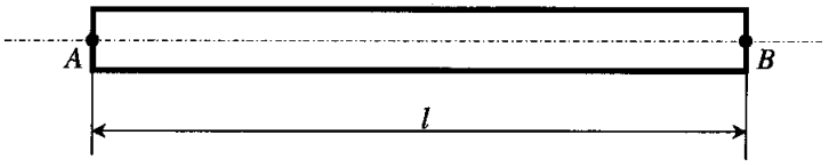

Figure 2.5: Two-noded beam element.

The fundamental concept underlying the finite element method involves representing the variable of interest using an approximating function, relying solely on the known variable values at the nodal points. In this approach, the overall location of a generic point is established through cubic polynomials in the x direction and linear polynomials in both the y and z directions. This enhancement is introduced specifically to augment the modelling capabilities along the x-axis, in terms of expressive power.

$$\boldsymbol{r} = \begin{bmatrix} r_1 \\ r_2 \\ r_3 \end{bmatrix} = \begin{bmatrix} a_0 + a_1x + a_2y + a_3z + a_4xy + a_5xz + a_6x^2 + a_7x^3 \\ b_0 + b_1x + b_2y + b_3z + b_4xy + b_5xz + b_6x^2 + b_7x^3 \\ c_0 + c_1x + c_2y + c_3z + c_4xy + c_5xz + c_6x^2 + c_7x^3 \end{bmatrix} \tag{2.3}$$

The polynomials have a total of 24 parameters. Consequently, the nodes of each element must have a total of 24 variables to fully determine such expressions. Each node is described by a column vector containing 12 coordinates, arranged as follows:

$$\boldsymbol{e}_j = \left[\boldsymbol{r}^T \quad \boldsymbol{r}_{,x}^T \quad \boldsymbol{r}_{,y}^T \quad \boldsymbol{r}_{,z}^T\right]_j^T, j = A, B, \tag{2.4}$$

Here, $\boldsymbol{r}$ represents the global position vector of the node, while $\boldsymbol{r}_{,\alpha}$ ($\alpha = x, y, z$) is the derivative of the position vector with respect to the α direction. By replacing the initial nodal coordinate values into the interpolating polynomial, the resultant shape function $\boldsymbol{S}$ of Eq. 2.2 can be derived. This shape function effectively establishes the correlation between the local coordinates and the global position of the generic point:

$$\boldsymbol{S} = \left[S_1\boldsymbol{I} \quad S_2\boldsymbol{I} \quad S_3\boldsymbol{I} \quad S_4\boldsymbol{I} \quad S_5\boldsymbol{I} \quad S_6\boldsymbol{I} \quad S_7\boldsymbol{I} \quad S_8\boldsymbol{I}\right], \tag{2.5}$$

where $\boldsymbol{I}$ is the 3×3 identity matrix and:

$$S_1 = 1 - 3\xi^2 + 2\xi^3, \quad S_2 = l(\xi - 2\xi^2 + \xi^3), \quad S_3 = l(\eta - \xi\eta), \quad S_4 = l(\zeta - \xi\zeta)$$
$$S_5 = 3\xi^2 - 2\xi^3, \qquad S_6 = l(-\xi^2 + \xi^3), \qquad S_7 = l\xi\eta, \qquad S_8 = l\xi\zeta$$

The non-dimensional quantities ξ, η, ζ are defined as:

$$\xi = x/l, \quad \eta = y/l, \quad \zeta = z/l,$$

The variable l is the length of the beam element in the undeformed configuration. It can be demonstrated that the shape function of Eq. 2.5 can represent any rigid body motion, including significant translations and rotations, as well as arbitrary deformation modes.

Figure 2.6 shows with an example of a beam fixed at its end and free to deform under its own weight. Structural properties of the beam, such as the Young Modulus, have been set to small values to simulate the properties of a rope-like body.

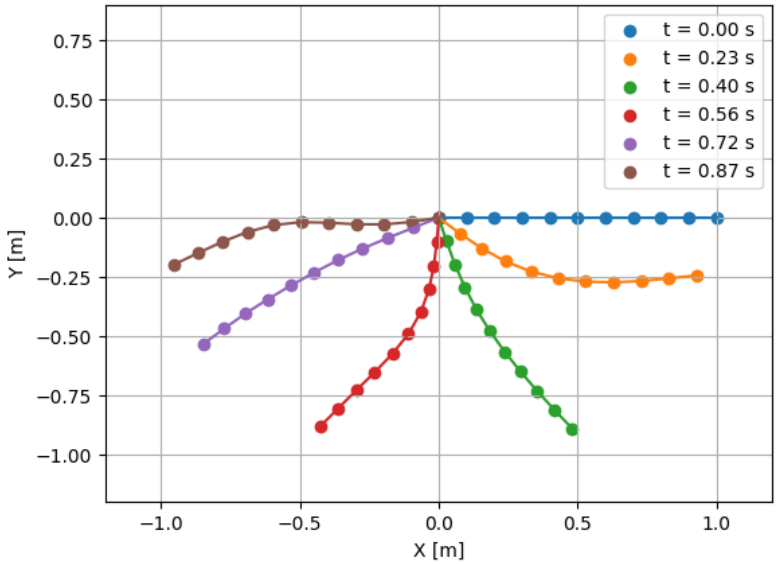

Figure 2.6: Simple rope swing, using 10 ANCF beam elements.

As evident from the simulation outcomes, the rope displays oscillatory patterns that align with the intuitive expectations. Nevertheless, even a basic test such as this, with a time frame of one second, demanded a significant amount of computational time.

Overall, this formulation offers a range of benefits for our application. Firstly, it operates without imposing any assumptions on body displacements, rendering it suitable for substantial deformations and strains. This is due to the formulation's capacity to offer a precise representation of multibody dynamics, as demonstrated in the work [27]. Moreover, the formulation maintains a constant mass matrix that can be solved analytically. This eliminates the need for recomputing the matrix at each time step, presenting a significant advantage. Additionally, as all variables are in the global reference frame, inertia forces can be directly calculated by multiplying the mass matrix with the vector of nodal accelerations within the global inertial frame. Furthermore, both centrifugal and Coriolis forces are nullified due to the use of a global, absolute frame. This prevents any inertial interaction between the extensive movement of the rigid body and the elastic deformation, differently to other formulations like the Floating Reference Frame. Incorporating constraint equations, such as hinge joints,

is straightforward; this involves sharing nodes between two bodies. More complex constraints can be included by the means of the Lagrange multipliers.

Nevertheless, there are a number of drawbacks. Implementing this method for simulation is intricate and time-consuming, necessitating expertise and comprehensive knowledge in creating a finite element simulation environment. The key disadvantage is that internal elastic forces exhibit high non-linearity, and the same expression is used for both small strains and large deformations. Consequently, the computational time remains consistent across small deflection and large deflection problems. The analytic expression of such forces is highly complex, and requires numeric integration procedures such as the Gaussian quadrature formulas [28]. Furthermore, modal order reduction often doesn't have a straightforward solution. While using fewer coordinates to define a node is possible, it leads to compromised accuracy and descriptive capabilities. For example, a common simplification involves using "cable elements" instead of "beam elements". This is done by reducing the node's degree of freedom for rotation around its own axis, failing to describe cross-sectional deformations. Such elements, termed "gradient deficient", employ only one gradient vector in the nodal coordinate vector. In the context of the IAC simulation application, disregarding torsional effects isn't feasible. The proof of concept simulation aims to assess the potential instability of the rope under torsional loads, primarily from the capturing device. However, longer ropes exhibit limited torsional stiffness, and the capturing device should ideally not undergo uncontrolled rotation around its axis. While the cable-like assumption has its limitations, it considerably accelerates computation, but the overall computational burden remains too heavy for our application.

In conclusion, this approach remains highly valid and necessitates further exploration, particularly in terms of developing a fast implementation strategy. Given that each element can be independently processed and subsequently connected via connectivity boolean matrices, parallel processing on separate computing cores can be performed at each time step.

2.2.4 Lumped Masses Models

In many practical scenarios, such as aerial refueling and underwater cable towing, as discussed earlier in the introductory section, the adoption of finite element methodologies becomes exceedingly computationally intensive and challenging to derive. As a result, a range of heuristic methods have been suggested, with the prevalence of approaches involving lumped masses and finite segments. Within this category of methods, the flexible body is discretized into lumped masses connected by rigid links. This approach offers the benefits of simplicity and efficiency in tackling the kinematics and dynamics of flexible bodies.

Ro and Kamman [29] introduced a model for the hoses employed in aerial refueling. They conceptualize it as a sequence of interconnected rigid links with ball-and-socket joints, subjected to predefined motions of the refueling aircraft (Fig. 2.7).

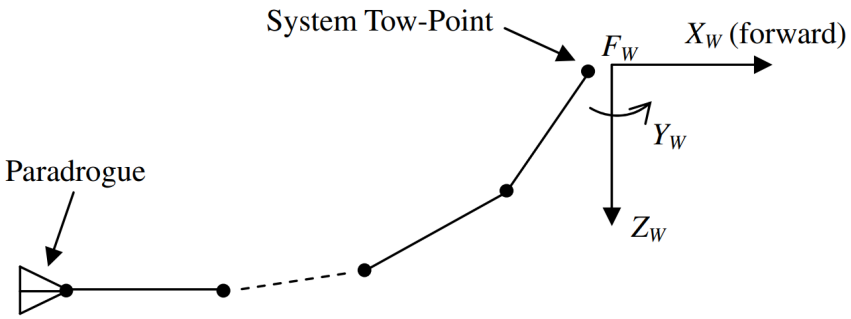

Figure 2.7: Overview of the modelling of the hose-drogue system (Source: [29]).

A similar configuration, involving a paradrogue positioned at the opposite end similar to the ACCD in our context, is adopted. The system's masses are concentrated at these joints. A comprehensive investigation is conducted to analyze the effects of aerodynamic loads, accounting for factors such as wake and turbulence. The equations of motion were derived from Newton's Laws, avoiding the need for a minimal set of variables to describe each element. Furthermore, constraint equations were integrated to ensure continuity among the elements. Given the problem's nature, opting for a recursive approach to describe element kinematics seems a logical choice. While they show high potential in terms of ensuring a suitable accuracy-computation trade-off, hose models lack important structural mechanics features. Generally, most of the models do not encompass a description of the hose elongation, since it can be assumed to be negligible in such applications. Moreover, a physics-based description of the stiffness and damping is not present.

Fritzkowski et al. expanded on this concept in various iterations of their work [30][31][32][33]. They introduced a chain-like model in which the rigid rope segments are connected via revolute joints. In their latest iteration, non-ideal joints are integrated, considering attributes like elasticity and dissipation. The approach presented by Fritzkowski et al. has proven to be promising for our application, and it has been used in past rope models employed by DLR. The modelling methodology appears to provide an adequate description of the underlying physics, while also allowing for a reasonably low computational load. However, the presented model is limited to the 2D case and lacks extensibility in terms of computing the new equations of motion. An essential requirement is for the model to encompass the 3D description. Consequently, their work cannot be directly applied. Furthermore, outcomes reveal that lumped masses models are susceptible to inducing chain-link oscillations within the hose dynamics, which are inappropriate for flexible bodies. Addressing these non-physical oscillations becomes necessary to achieve a realistic description of the dynamics of the system.

These challenges will be addressed in Section 3 of the present work, where a novel multibody approach, inspired by the work of Fritzkowski et al., will be proposed.

3 Modelling Methodology

The following section presents the new modelling approach to describe the rope dynamics. The primary objective is to derive closed-form expressions for the equations of motion, enabling direct implementation in software for use in the simulation environment. A MBS will be proposed, involving the discretization of the rope into numerous rigid bodies constrained to be connected at their ends. The formulation will employ a minimal set of state variables, leveraging the benefits of the recursive formulation in multibody problems. A set of features will be added, to model rope properties such as the bending stiffness and the elongation. Ways to incorporate external actions will be examined, such as the handling of rheonomous constraints and aerodynamic forces. The energy balance for the system is presented, and will be used in the following section as a procedure to validate the correctness of the model. Ultimately, a final expression for the equations of motion will be proposed, as a direct function of the number of elements used in the rope discretization.

3.1 Environment Description

In the context of the IAC manoeuvre, the main goal is to simulate the dynamics of the capturing system, composed of the rope and the ACCD attached to its end. The main focus of this dissertation is to derive the equations of motion for the rope dynamics, which can later be utilized in larger MBS. Consequently, the dynamics of the capturing device will not be explicitly described. In the subsequent chapter, IAC simulations will be performed, considering the ACCD as a lumped mass at the end of the rope and incorporating it within the rope model itself.

The general configuration of the environment is illustrated in Figure 3.1. One end of the rope is fixed to the towing aircraft, which undergoes a pre-defined motion. For simplicity, the aircraft is assumed to begin in cruise condition, aligning its motion with the horizontal relative airstream. As it will be discussed in subsection 4.1.3, if the aircraft's velocity remains constant, no inertia forces will be applied to the rope. The ACCD is attached to the other end of the rope, and they are constrained to share the same point. The underlying constraint equation ensures that they have the same acceleration at that point. Through the simulation of the rope dynamics, the acceleration of the rope's bottom end can be estimated and imposed to the ACCD motion. Consequently, the position and velocity of the ACCD at the connection point become fixed. Thus, accurate modeling of the rope dynamics is crucial in tuning the control strategy, enabling the ACCD to approach the RLV and successfully mate with it. Subsequent stages following the connection with the RLV will be the subject of future research.

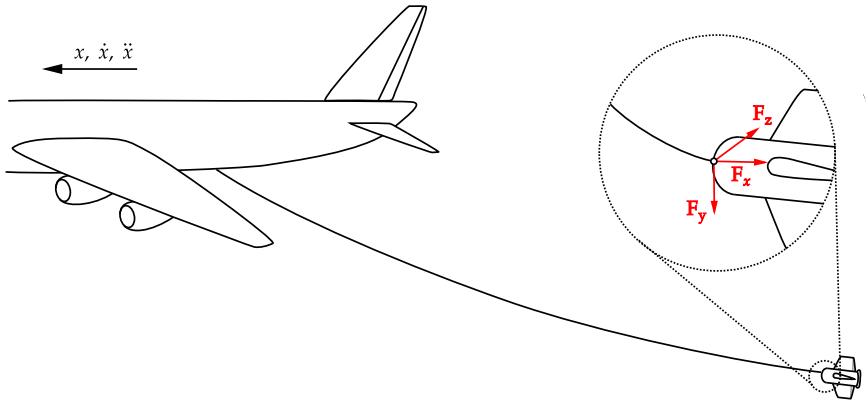

Figure 3.1: Schematic representation of the rope and ACCD capturing system, attached to the towing aircraft.

3.2 Kinematic Description

The rope modelling starts with a description of the kinematic. It is reasonable to establish the origin of the global reference frame as that of the aircraft, which effectively enforces a fixed joint constraint. This approach enables the description of the rope's relative kinematics with respect to the aircraft. When the TA maintains a constant velocity, the aircraft reference frame becomes inertial. In this simplified scenario, there is no need to introduce inertia forces in the rope model. However, during the IAC procedure, the aircraft will often decelerate and accelerate to align with the RLV. Consequently, the rope model must be able to incorporate the inertia effects of such changes in motion. As introduced in Section 2, the general idea for the rope

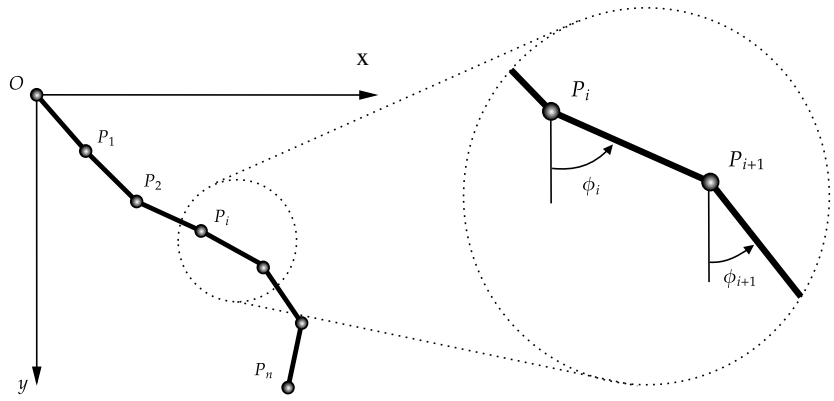

Figure 3.2: Discretization of the rope as a chain of rigid bodies.

modelling is inspired on the work of Fritzkowski et al. [30]. They present a 2D

model, which cannot be directly applied to our specific application. This thesis work aims at expanding their framework to encompass a complete 3D environment. Their modelling approach is shown in Figure 3.2.

The rope is discretized into n segments of length L and mass m each, connected by frictionless joints. Assuming that each element behaves like a rigid cylindrical rod, the discrete model of the rope resembles a system of multiple physical pendulums. Generalized angular coordinates are introduced, which represent the global angle ϕ_i that an element has with respect to the vertical axis. While this representation is intuitive in a 2D setting, an additional angle, denoted as ψ, is required to describe the bending of the rope in the third direction. This ψ angle is incorporated in the element's description following a spherical scheme (Figure 3.3).

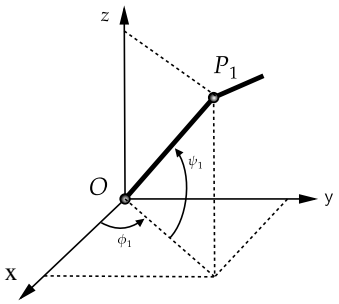

Figure 3.3: 3D description of a rope element using a spherical set of angles.

In this work, we will refer to ϕ angles as "polar" angles, and to ψ angles as "azimut" angles. In fact, polar angles are measured from the zenith (vertical direction), while the azimuth ones describe the orientation in the reference horizontal plane (x-z in this reference frame) [34].

The 3D Cartesian position of one point can be obtained as:

$$\begin{cases} x_1 = L \cdot \cos\psi_1 \cdot \sin\phi_1 \\ y_1 = L \cdot \cos\psi_1 \cdot \cos\phi_1 \\ z_1 = L \cdot \sin\psi_1 \end{cases}$$

Starting from the first element, all the others are attached in a chain like model. Therefore, the Cartesian coordinates of the i_{th} element (most specifically, its centre of mass) may be written as follows:

$$\begin{aligned} x_i(t) &= x_0(t) + \frac{L}{2}\sum_{j=1}^{i-1}\cos\psi_j \cdot \sin\phi_j + \frac{L}{2}\cos\psi_i \cdot \sin\phi_i \\ y_i(t) &= y_0(t) + \frac{L}{2}\sum_{j=1}^{i-1}\cos\psi_j \cdot \cos\phi_j + \frac{L}{2}\cos\psi_i \cdot \cos\phi_i \\ z_i(t) &= z_0(t) + \frac{L}{2}\sum_{j=1}^{i-1}\sin\psi_j + \frac{L}{2}\sin\psi_i \end{aligned} \tag{3.1}$$

The components of the linear velocity and acceleration of the *i*th segment in the *X, Y, Z* directions are computed by simply derivating Eq. 3.1 with respect to time:

$$\begin{aligned} v_{x_i}(t) &= \frac{dx_i(t)}{dt}, \quad a_{x_i} = \frac{d^2x_i(t)}{dt^2} \\ v_{y_i}(t) &= \frac{dy_i(t)}{dt}, \quad a_{y_i} = \frac{d^2y_i(t)}{dt^2} \\ v_{z_i}(t) &= \frac{dz_i(t)}{dt}, \quad a_{z_i} = \frac{d^2z_i(t)}{dt^2} \end{aligned} \tag{3.2}$$

These expressions can be written in terms of the generalized coordinates and their derivatives. These formulas will also be used in the IAC simulation, since the acceleration of the last node of the rope is shared with the ACCD. The acceleration of the last node will be fed to the ACCD model to couple the two systems.

3.3 Dynamics Description

In order to derive the equations of motion, the Euler-Lagrangian approach is used. This requires the definition of the *lagrangian*, a function of the kinetic and potential energy of the system [35]:

$$\mathcal{L} = T - V \tag{3.3}$$

where T and V are respectively the kinetic and potential energy.

The kinetic energy is defined as following, using König's theorem:

$$T = \frac{1}{2}m\sum_{i=1}^{n} v_i^2 + \frac{1}{2}I\sum_{i=1}^{n} \dot{\phi_i}^2 + \frac{1}{2}I\sum_{i=1}^{n} \dot{\psi_i}^2 \tag{3.4}$$

In Eq. 3.4, m is the mass of the single rope element. v_i is the linear velocity of the center of mass of the i_{th} element. I is the moment of inertia of the element, which is assumed to be a cylindrical rod. $\dot{\phi_i}$ and $\dot{\psi_i}$ are the angular velocities, derivatives of the polar and azimuth angles used as generalized coordinates.

The potential energy of the system V is given by:

$$V = -mg\sum_{i=1}^{n} y_i \tag{3.5}$$

In Eq. 3.5, g is the gravitational acceleration, while y_i is the y-position of the i_{th} element center of mass. In this work g will mostly assume a constant value, since we assume to be in cruise flight, but it in the later stages of the IAC validation one must modify its value according to the environmental conditions.

The Lagrange equations of motion can be written as:

$$\frac{d}{dt}\left(\frac{\partial \mathcal{L}}{\partial \dot{q}_i}\right) - \frac{\partial \mathcal{L}}{\partial q_i} = Q_i, \quad i = 1, 2, ..., k \tag{3.6}$$

where Q_i are the generalized forces applied to the system, which will be described more in detail in the following subsections. We will refer to them as the non-lagrangian

components. The number of equations is equal to number of generalized coordinates used in the description of the chain. A polar and an azimuth angle were used to characterize each element, so the variables will be $2n$ in total.

The power of the Lagrange equations consists in allowing for a systematic computation of the equations of motion, without the necessity of going through a detailed geometrical description of the problem setting. For systems such as the proposed model, where there is a large number of simple bodies constrained to be together, it allows to compute the minimal set of equations. In fact, the coupling between generalized coordinates that appears in the constraint equations, is automatically encoded in the final set of equations.

3.3.1 Bending Stiffness

Modelling the rope only as a simple multiple-physical pendulum leads to a disordered, extremely chaotic system, as it is shown in the work from [30]. The single elements are completely free to rotate around the connecting joints, thus the system is able to describe the wave-like effects that are typical of the dynamics of whips. However, when the energy transmission is too large or fast, elements are free to perform non-natural, unrestricted rotations.
Therefore, it is necessary to introduce transverse elasticity features in the model. This is done by introducing bending stiffness at the joints, by the means of the concept of spiral springs [32]. Identical, mass-less springs with stiffness K_t are placed in each of the joints, as shown in figure 3.4. These elements will apply a torque opposite with respect to the curvature of the elements.

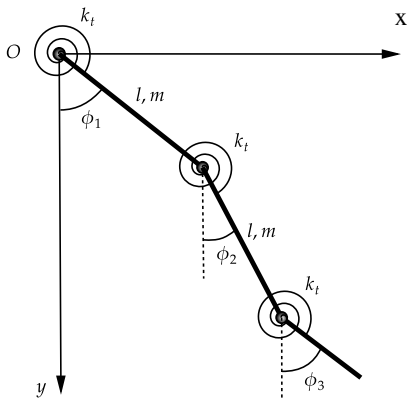

Figure 3.4: Rope discrete model with bending stiffness at the joints.

The bending stiffness torque can be defined as a direct function of the body local curvature. A closed-form expression for the curvature can be obtained as a function of

the parametric representation of the curve $\boldsymbol{\gamma}(s) = f(x(s), y(s), z(s))$ [36]:

$$R = \frac{|\boldsymbol{\gamma}'|^3}{\sqrt{|\boldsymbol{\gamma}'|^2|\boldsymbol{\gamma}''|^2 - (\boldsymbol{\gamma}' \cdot \boldsymbol{\gamma}'')^2}} \tag{3.7}$$

Equation 3.7 shows that the reference curve shall be twice differentiable. The goal is to find an expression of the curve in the proposed discretized model. We first consider a sequence of two elements of the rope in a simplified 2D setting, in a local coordinate system xy (Figure 3.5). Polar angle ϕ is defined using the convention used in the kinematics description.

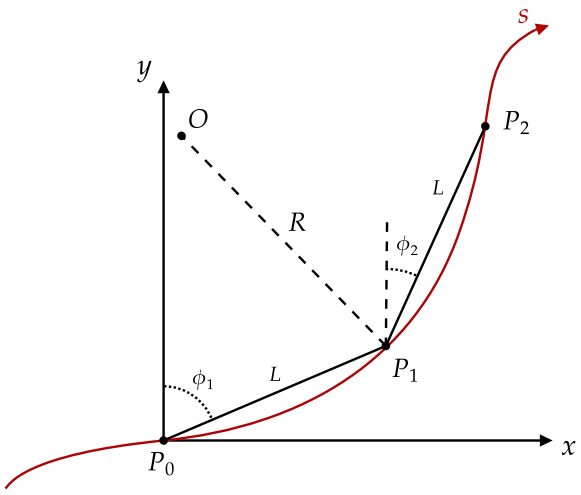

Figure 3.5: Curvature of a generic discretized curve.

Equation 3.7, valid for a generic curve in space, assumes a simplified expression in a 2D environment:

$$R = \frac{|\gamma'|^3}{\det(\gamma', \gamma'')} = \frac{\left(\dot{x}^2 + \dot{y}^2\right)^{\frac{3}{2}}}{\dot{x}\ddot{y} - \dot{y}\ddot{x}} \tag{3.8}$$

The computation of the derivatives must take into account the discretization in sub-elements. Supposing one wants to estimate the curvature R at point P_1, we consider the two adjacent rigid elements. To compute derivatives, we rely on a discretization of the rope in multiple segments. In the presented coordinate system, the positions of the points P_0, P_1, P_2 can be specified as follows:

$$\begin{aligned} &x_0 = 0, \quad y_0 = 0 \\ &x_1 = L \sin\phi_1, \quad y_1 = L \cos\phi_1 \\ &x_2 = L\ (\sin\phi_1 + \sin\phi_2)\,, \quad y_2 = L\ (\cos\phi_1 + \cos\phi_2) \end{aligned} \tag{3.9}$$

The derivatives of x and y, with respect to the curvature coordinate, can be approximated

by using the central difference schemes:

$$\begin{aligned} \dot{x} &= \frac{x_2 - x_0}{2\,L}, \quad \dot{y} = \frac{y_2 - y_0}{2\,L} \\ \ddot{x} &= \frac{x_2 - 2x_1 + x_0}{L^2}, \quad \ddot{y} = \frac{y_2 - 2y_1 + y_0}{L^2} \end{aligned} \tag{3.10}$$

Substituting the formulas for the derivatives in Eq. 3.8, an expression for the radius of curvature is obtained:

$$R = -\frac{L}{2}\cos(\theta/2)\ \cot(\theta/2) \tag{3.11}$$

where $\theta = \phi_2 - \phi_1$ is a generalized coordinate which describes the relative rotation.

The bending moment M is computed using the basic expression for the strength of materials [37]:

$$M = \frac{K_t}{R} = -\frac{2K_t}{L}\frac{\tan(\theta/2)}{\cos(\theta/2)} \tag{3.12}$$

where K_t is the flexural rigidity. A shape of the resulting nonlinear spring characteristic is shown in figure 3.6:

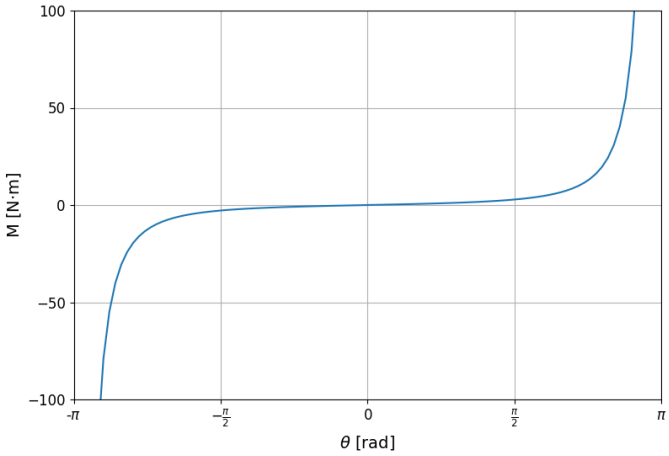

Figure 3.6: Non-linear bending stiffness used in the model.

It must be noted that if two elements tend to have a relative rotation $\theta = \pi$, the elastic force M will grow infinitely. Consequently, the curvature expression prevents unnatural, full rotation at the joints.

To apply this concept to the proposed model, it is sufficient to implement Equation 3.12 in all i_{th} joints:

$$M_i = \frac{K_t}{R} = -\frac{2K_t}{L}\frac{\tan(\theta_i/2)}{\cos(\theta_i/2)} \tag{3.13}$$

θ_i is specified as following:

$$\theta_i = \begin{cases} \phi_i & \text{for } i = 1 \\ \phi_i - \phi_{i-1} & \text{for } i = 2, 3, ..., n \end{cases}$$

The virtual work done by the spring moments at the joints can be expressed with respect to the generalized coordinates θ_i:

$$\delta W = M_1 \delta\theta_1 + M_2 \delta\theta_2 + \cdots + M_n \delta\theta_n \tag{3.14}$$

From Equation 3.14, it is straightforward to obtain an expression of the related generalized forces associated with the polar angle ϕ_i:

$$Q_i^M = \frac{\partial W}{\partial q_i} = \begin{cases} M_i - M_{i+1}, & \text{for } i = 1, 2, \cdots, n-1 \\ M_i, & \text{for } i = n \end{cases} \tag{3.15}$$

The same reasoning can be applied to the azimuth angle ψ, which describes the bending in the xz plane.

A model of the rope bending which separately handles the two angles is a simplification. A stiffness model which starts from a 3D description of the curvature of the system is more accurate from a physical perspective. In this work, a 2D model was used, because of the simplicity of the analytic expression. However, it effectively decouples the two angles, which are actually tightly correlated to each other in the kinematic description of the system. A closed-form expression for the curvature in a three dimension space exists, but it leads to a very complex equation. An analysis on the impact of the adoption of this simplified approach is left for future work.

3.3.2 Viscous Damping

The addition of the transverse elasticity, compared with the multiple physical pendulum, eliminates full rotations for the segments. However, as can be seen from Fritzkowski's work, the contribution of the rotational kinetic energy only increases with the introduction of the stiffness [32]. As a consequence, the chaotic-looking dynamics does not experience a reduction in strength, since the stabilizing activity of the spring induces only further rotational oscillations.

It is crucial to replace simple springs with viscoe-lastic ones, to damp out the transverse oscillations. Therefore, viscous dampers of a damping coefficient c are added to the rope joints [33]. Similar to the bending stiffness description, the problem is tackled by splitting the problem in two planes x-y and x-z (Figure 3.7). Therefore, each set of angles is addressed individually.

Dissipative, generalized forces can be derived from the Rayleigh dissipation function [35]:

$$R = \frac{1}{2} c \sum_{i=1}^{n} \dot{\theta}_i{}^2 \tag{3.16}$$

where $\dot{\theta}_i$ represents the relative angular velocity:

$$\dot{\theta}_i = \begin{cases} \dot{\phi}_i & \text{for } i = 1 \\ \dot{\phi}_i - \dot{\phi}_{i-1} & \text{for } i = 2, 3, ..., n \end{cases}$$

The generalized forces with respect to the polar angles are given by:

$$Q_i^D = -\frac{\partial R}{\partial \dot{\phi}_i}, \quad i = 1, 2, \cdots, n \tag{3.17}$$

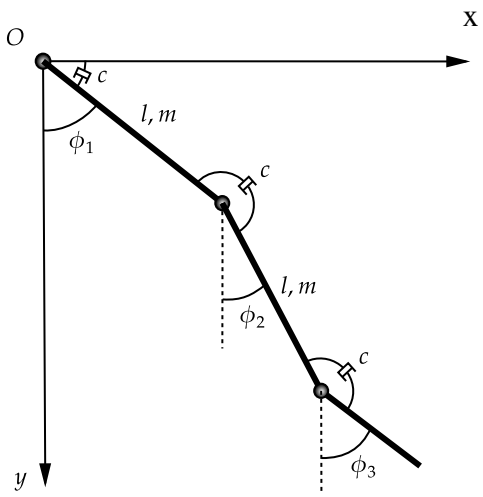

Figure 3.7: Rope discrete model with viscous damping at the joints.

Which leads to the final expression:

$$Q_i^D = \begin{cases} c\left(\dot{\theta}_{i+1} - \dot{\theta}_i\right) & \text{for } i = 1, 2, \cdots, n-1 \\ -c\,\dot{\theta}_i & \text{for } i = n \end{cases}$$

As in the bending stiffness description, this approach is repeated in the x-z plane to find an expression in terms of the azimuth angle.

It cannot be overstated the importance of the damping in allowing the simulation to show realistic results and run in a reasonable timestep. The original work by Fritzkowski et al. does not use damping in the modelling of the system, and it is evident how the simulation becomes unstable after a single rope swing. A further comparison of the model with and without the effect of damping will be performed in Section 4.1.3.

The values for the damping coefficient of such a formulation cannot be found directly in the rope material datasheets or other types of benchmarks. Experimental data is necessary to find a proper estimate. This information was not available during the work, and cannot be found in the literature. Therefore, a sensitivity analysis on the value of this parameter was performed. In the simulations, we used coefficients which showed to produce a rope behaviour which is intuitively reasonable. Nevertheless, it is crucial to produce experimental results to find suitable values for this coefficient.
It was observed that with larger rope mass, the effect of damping would get negligible if the same coefficient is used. For this reason, it is appropriate to employ the empirical assumption of Rayleigh Damping, which is used in the context of Finite Element Methods. It assumes that the damping coefficient is a linear combination of the system's mass and stiffness:

$$C = \alpha M + \beta K$$

where α and β are empirical coefficients. The estimation of such parameters is not trivial. For slender flexible bodies, it can be assumed that the stiffness has a much

smaller impact compared to the mass. In this work, the final damping coefficient is de facto proportional only to the rope mass. In this way, the future experimental validation will just tackle the estimation of a single coefficient. For the rest of the present work, we will refer to α as the generic c damping coefficient.

While applying damping to relative velocity is key to keep the simulation stable, in some cases it is not enough to completely damp out the motion of the system overtime. In fact, the full dissipation of low frequency oscillations requires excessive time, which might differ from experimental data. Therefore, this may suggest to apply another source of damping directly to the absolute angular velocities. A dedicated analysis is left for future work, since experimental data is first needed to validate the rope model.

3.3.3 External Forces

External forces are incorporated in the non-lagrangian component of Equation 3.6. Forces will be input to the model, mostly expressed in Cartesian coordinates. Therefore, they must be converted into generalized forces which refer to the angular coordinates used in the presented model. The virtual work of the generic external force $\boldsymbol{F}$, applied in point P, is:

$$\delta W = \boldsymbol{F} \cdot \delta \boldsymbol{r}_p$$

where $\boldsymbol{r_p}$ is the position of point P in Cartesian coordinates. Applying the partial differentation chain rule, an expression for the generalized force $\boldsymbol{Q}$ is obtained.

$$\delta W = \boldsymbol{F} \cdot \delta \boldsymbol{r}_p = \boldsymbol{F} \frac{\partial \boldsymbol{r}_p}{\partial \boldsymbol{q}} \partial \boldsymbol{q}$$

$$\boldsymbol{Q} = \boldsymbol{F} \cdot \frac{\partial \boldsymbol{r}_p}{\partial \boldsymbol{q}} \tag{3.18}$$

r_p is the Cartesian position of point P, which it can be supposed to be found on the j_{th} element. It follows that its position is only described by coordinates ϕ_i and ψ_i with index $i < j$. Generalizing from Equation 3.18, the force will only affect the element where it is applied and the ones that can be found previously in the chain.
Equation 3.18 can be rewritten as follows:

$$\boldsymbol{Q} = \begin{bmatrix} f_x \\ f_y \\ f_z \end{bmatrix}^T \cdot \mathrm{T} \tag{3.19}$$

where f_x, f_y, f_z are the Cartesian components of the force, while T is the matrix which allows the transformation to the generalized coordinates of the system. In detail:

$$\mathrm{T} = \begin{bmatrix} \frac{\partial \boldsymbol{r}_{p_x}}{\partial q_1} & \frac{\partial \boldsymbol{r}_{p_x}}{\partial q_2} & \cdots & \frac{\partial \boldsymbol{r}_{p_x}}{\partial q_k} \\ \frac{\partial \boldsymbol{r}_{p_y}}{\partial q_1} & \frac{\partial \boldsymbol{r}_{p_y}}{\partial q_2} & \cdots & \frac{\partial \boldsymbol{r}_{p_y}}{\partial q_k} \\ \frac{\partial \boldsymbol{r}_{p_z}}{\partial q_1} & \frac{\partial \boldsymbol{r}_{p_z}}{\partial q_2} & \cdots & \frac{\partial \boldsymbol{r}_{p_z}}{\partial q_k} \end{bmatrix}$$

where k is the toal number of generalized coordinates. As aforementioned, it is sufficient to only compute the columns of the T matrix until the j_{th} element, since the force has no effect on the coordinates which describe elements following the application point.

So far, only punctual forces have been considered. Distributed forces along the rope length, such as gravity or aerodynamic effects, can be modelled by individually applying their expression to the centers of mass of all elements. Thus, it is possible to use the same reasoning used for lumped forces, by simply looping over all elements. A different description must be considered for punctual forces applied at the top end. The position of the rope first node is not described by any generalized coordinate, so following the previous description such forces would have no impact on the system. However, it must be mentioned that the rope has been modelled to have its top node constrained in a specific point. Therefore, it is more reasonable to impose an acceleration for this node, rather than an external force. This is the case of the IAC mission, since the rope is constrained to the aircraft on its top end. A more detailed discussion can be found in the following section.

3.3.4 Rheonomous Constraints

In the IAC mission, the rope is attached to the towing aircraft at its top end. The reference frame of the rope body describes the relative position with respect to the aircraft, and its origin is fixed in the connection point. As it can be observed from Equation 3.1, the origin of the rope reference frame is constrained to have the same motion of the aircraft. This acts like a *rheonomous constraint* for the system, because the time variable appears explicitly in the equation [35]. Equation 3.1 is used in the computation of the Lagrange equations, which involves partial derivatives with respect to the coordinates velocities and the time variable. In the final set of equations, the contribution of rheonomous constraints to the non-lagrangian of the system is:

$$\boldsymbol{q} = -m\,\boldsymbol{a_0}(t)$$

where $\boldsymbol{a_0}(t)$ is the acceleration of the rope first node. It can be thought as an apparent inertia force applied to all elements that acts in the opposite direction with respect to the reference frame acceleration. The method used to apply this force to individual rope segments is analogous to how distributed forces are applied to the rope. Generally, only accelerations of the TA will appear in the equations, not position or velocity. This is reasonable, as describing the relative position with respect to a fixed frame does not require to consider apparent forces when the frame is inertial. In the IAC mission, the aircraft reference frame cannot be considered as inertial, if the TA undergoes any kind of acceleration. While this study focuses on cruise flight condition, it must also allow the model to depict mission phases like the formation flight and pull-up maneuvers. Consequently, the rope model needs to encompass the influence of inertia forces, arising from changes in TA motion over time.

3.3.5 Aerodynamic Effects

The context of the IAC mission requires the implementation of a drag model for the rope body. Aerodynamic effects are analyzed by describing rope elements individually. The analytical expressions for drag and lift forces are as follows [38]:

$$\begin{aligned} F_D &= \frac{1}{2} C_D \rho A u^2 \\ F_L &= -\frac{1}{2} C_L \rho A u^2 \end{aligned} \tag{3.20}$$

Lift force comes with a negative sign to match the reference frame of the model, which points downwards. C_D and C_L are the drag and lift coefficients, which can be obtained from the angle of attack of the body. ρ is the mass density of the fluid, which will be input from the atmosphere model. A is the reference area of the body. In this case, the rope cross-section will be used. Finally, u is the velocity of the flow relative to the object. The proposed model effectively computes the relative velocity of the rope with respect to the aircraft, so this must be added to the TA reference velocity. Not only, effect of wind and aircraft wake must be taken into account as well.
The drag and lift coefficients were estimated using J.H. Lee's work (Figure 3.8), which describes the dynamics of ropes in underwater structures [39].

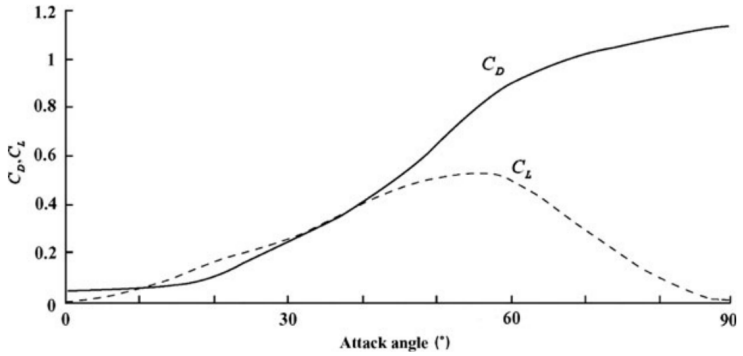

Figure 3.8: Drag coefficient (C_D) and lift coefficient (C_L) as a function of the angle of attack (Source: [39]).

Each element is considered to be cylinder-like, and the coefficients value is a function of the angle of the rod angle of attack with respect to the airflow. However, the proposed rope model describes the position in a 3D setting, so the angle of attack must be chosen with care. In the generalized coordinates used in the model description, polar angles ϕ describe the inclination of the rope element with respect to the horizontal line. If the aircraft is in cruise-flight condition, this angle is a natural choice for the angle of attack with respect to the airflow. However, it must be also considered the effect of the azimuth ψ, which represents the sideslip with respect to the aircraft reference.

The element actual angle of attack can be visualized by analyzing the plane created by the direction of the element and the x direction, which is supposed to be the one of the airflow (Figure 3.9) [40].

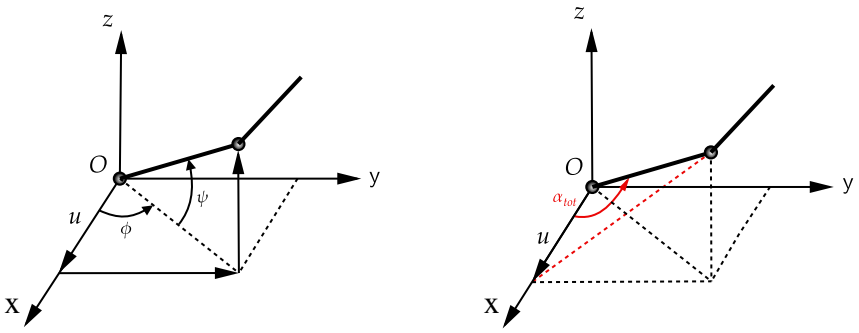

Figure 3.9: Derivation of a total angle of attack, to be used in the drag model.

α_{tot} is the *total* angle of attack. Since the element orientation is described using spherical coordinates, it is straightforward to compute the expression for such angle.

$$\begin{aligned} u &= v_{\text{inf}} \cdot \cos\alpha_t \\ u &= v_{\text{inf}} \cdot \cos\alpha \cdot \cos\beta \end{aligned} \quad \rightarrow \alpha_t = \cos^{-1}\left(\cos\alpha \cdot \cos\beta\right) \tag{3.21}$$

From the total angle of attack, it is possible to retrieve the drag and lift coefficients for each rope element.

Finally, the aerodynamic forces, expressed in Cartesian components, will be transformed to generalized forces following the reasoning described in Section 4.1.2.

Generally, in the final IAC simulation, it can be observed that the rope aerodynamics is negligible compared to the other forces that are in play. The drag of the ACCD attached to its end already shadows the contribution of the rope drag, which would otherwise be more relevant if the rope was deployed by itself.

3.3.6 Modelling of Rope Elongation

Ropes are very flexible bodies capable of sustaining high loads, while exhibiting relatively large axial deformation. A primary goal of the IAC simulation is to examine whether the rope is capable of handling the loads during the maneuver. Therefore, the model shall include a feature to estimate the rope tension and elongation. The rope has been discretized into a chain of rigid bodies, rigidly connected at the joints. It is not trivial to introduce the modelling of elongation in such a system.

A straightforward approach is presented in a further work of Pawel Fritzkowski, the author who first proposed a multibody approach for ropes [31]. The simple 2D model of the rope is expanded, by enabling the rigid segments to change their length. This is done by introducing an extra degree of freedom $s_i(t)$ to each element, which describes its elongation at a given time instant. As it can be observed from Figure 3.10, the modelling is performed in a simple spring-damper conception. The rods length L becomes effectively the natural length of the spring, whose axial stiffness and damping coefficients are expressed by k and c_k. The kinematics of the system

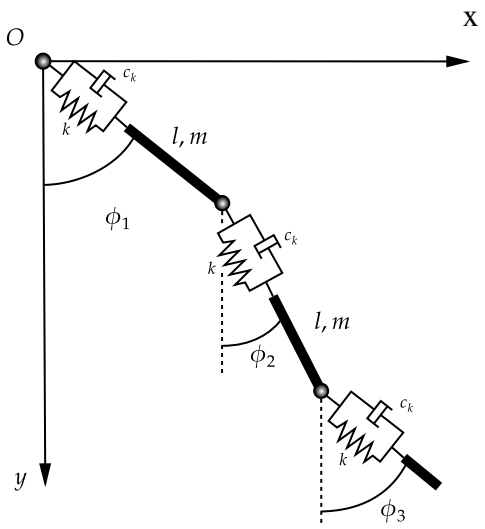

Figure 3.10: Rope discrete model with linear visco-elastic elements connected to each segment.

will be different from Equation 3.1. The position of the center of mass of the ith body segment, in the Cartesian plane, can be written as:

$$
\begin{aligned}
x_i(t) &= x_0(t) + \sum_{j=1}^{i-1} \left(\frac{L}{2} + s_j(t) \right) \cos\psi_j \cdot \sin\phi_j + \frac{L}{2} \cos\psi_i \cdot \sin\phi_i \\
y_i(t) &= y_0(t) + \sum_{j=1}^{i-1} \left(\frac{L}{2} + s_j(t) \right) \cos\psi_j \cdot \cos\phi_j + \frac{L}{2} \cos\psi_i \cdot \cos\phi_i \\
z_i(t) &= z_0(t) + \sum_{j=1}^{i-1} \left(\frac{L}{2} + s_j(t) \right) \sin\psi_i + \frac{L}{2} \sin\psi_i
\end{aligned}
\tag{3.22}
$$

The derivation of the equations of motion follows the same reasoning as before, but adding the springs energy to the potential energy term. The equations of motion presented in Fritzkowski's work are already rather complex, only covering the 2D case. Expanding the presented elastic model to a 3D environment leads to a very convoluted set of equations. The model would add a third coordinate to all elements, which is tightly correlated to the other two in the formulation of the kinematics. In this context, it is challenging to find a closed-form expression as direct function of the number of elements.

Not only, the adoption of an elongation term at every element leads to an extremely chaotic system, prone to be unstable for larger timesteps in the integration. The oscillating behaviour of a single spring affects the motion of all following elements. For longer chains of elements, this effect adds up and leads to unstable configurations or unrealistic oscillations. The addition of the damping element helps with stability of

the system, but it is still challenging to maintain the simulation stable with a reasonable timestep.

As a consequence, a simplified model will be proposed. The main idea consists in introducing a single, linear visco-elastic element at the beginning of the chain, as sketched in Figure 3.11.

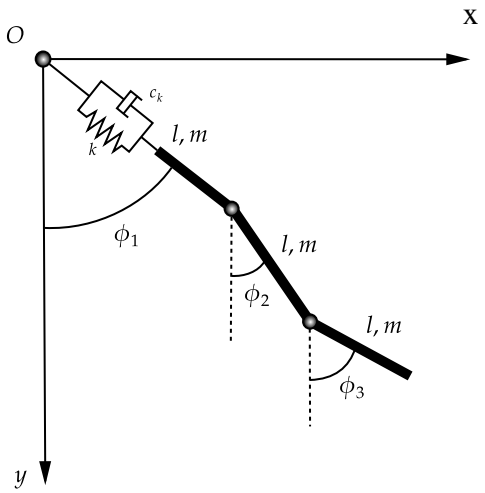

Figure 3.11: Rope discrete model with linear visco-elastic element at the top node.

This component is assumed to model the elongation of the whole rope, by setting its axial stiffness coefficient using the relation [37]:

$$k_a = \frac{EA}{L_{tot}}$$

where E is the Young modulus of the material. This is a substantial simplifying assumption, but it can be reasonable under some perspectives. An estimate of the elongation is needed in structural tests, when different loads are applied to the rope. In the IAC mission, external actions are likely to make the rope assume a straight configuration, because of heavy stresses like the RLV drag. In this scenario, a single linear spring can approximately describe the rope total elongation, since the latter will lie in a single direction. Further investigations regarding the possibility to implement a spring at each element is left for future work.

3.4 Energy Balance

A correct modelling implies that the energy balance of the system shall be coherent. As it will be argued in Section 4, analyzing at the energy balance is the premiere way to verify the model, since experimental validation is problematic and requires dedicated effort. Hereafter the methodology used in the simulations will be discussed.

The objective is to verify that the law of conservation of mechanical energy holds. In other terms, the variation in the mechanical energy U of the system must be exactly

equal to the work done by non-conservative actions. The mechanical energy of the system can be written as:

$$U = T + V \tag{3.23}$$

T and V, respectively the kinetic and potential energy of the system, were defined in Section 3.3.
The work done by non-conservative actions at each time step is equal to:

$$\delta W_{ext} = \sum_{i=1}^{n} Q_{ext_i}\, dq_i + \sum_{i=1}^{n} Q_{D_i}\, d\theta_i + \sum_{i=1}^{n} Q_{el_i}\, d\theta_i \tag{3.24}$$

where q_i represents the generalized coordinate of the set $[s, \phi_i, ..., \psi_i, ...]$, while θ_i is the generalized coordinate introduced in Section 3.3.1. Q_{ext_i} is the sum of all generalized external forces for coordinate q_i, discussed in section 4.1.2. Q_{D_i} is the damping generalized force associated with coordinate q_i. The last term represents the work performed by the bending stiffness.

For implementation purposes, since the infinitesimal variation can be written as $dq = \dot{q}dt$, we can rewrite the previous expression as follows:

$$\delta W_{ext} = \left(\sum_{i=1}^{n} Q_{ext_i}\, \dot{q}_i + \sum_{i=1}^{n} Q_{D_i}\, \dot{\theta}_i + \sum_{i=1}^{n} Q_{el_i}\, \dot{\theta}_i \right) dt \tag{3.25}$$

All these quantities are computed in the calculation of the equations of motion, since dt is the integration time step and $\dot{q}_i, \dot{\theta}_i$ are the velocities of the generalized coordinates.

The final energy balance can be summarized as follows:

$$\Delta U - \int_S \delta W_{ext} = 0 \tag{3.26}$$

In Section 4, this difference will be computed at each time step. While the theoretical value would be zero, small deviations are likely to occur because of numerical error. Therefore, the residual computed in Eq. 3.26 will be effectively considered as the error cumulated in the integration step. If this assumption is true, then one might expect this quantity to get smaller with the use of a lower timestep or a higher order integrator. Additional discussions will be presented within the context of the simulation results.

3.5 ODE System

The final Lagrange equations (Eq. 3.6) assume a rather complex and convoluted expression. However, it is still possible to write set of equations in the linear, explicit form that is typical of mechanical systems:

$$\boldsymbol{M}(\boldsymbol{q})\ddot{\boldsymbol{q}} = \boldsymbol{f}(t, \boldsymbol{q}, \dot{\boldsymbol{q}}) \tag{3.27}$$

where:

$$\boldsymbol{M}(\boldsymbol{q}) = \begin{bmatrix} m_{1,1} & m_{1,2} & \cdots & m_{1,k} \\ m_{2,1} & m_{2,2} & \cdots & m_{2,k} \\ \vdots & \vdots & \ddots & \vdots \\ m_{k,1} & m_{k,2} & \cdots & m_{k,k} \end{bmatrix}, \quad \boldsymbol{f} = \begin{bmatrix} f_1 \\ f_2 \\ \vdots \\ f_k \end{bmatrix}, \tag{3.28}$$

$\boldsymbol{M}(\boldsymbol{q})$ and $\boldsymbol{f}(t, \boldsymbol{q}, \dot{\boldsymbol{q}})$ will be respectively referred to as mass matrix and right-hand side of the system. k represents the total number of generalized coordinates used in the kinematics formulation. It is equal to $2n$+1: n polar angles, n azimuth angles and the elongation variable. Both the entries of the mass matrix $m_{i,j}$ and the components of the right-hand-side f_i are not constant, so they must be evaluated at each time step. The full description of the mass matrix and the right-hand side can be found in Appendix A.

In order to integrate the equations of motion, the system must be transformed to first-order. This is done by introducing variables for the derivatives of the generalized coordinates: $\boldsymbol{u} = \dot{\boldsymbol{q}}$. The final first-order ODE for the model can be written as:

$$\hat{\boldsymbol{M}}(\boldsymbol{X})\dot{\boldsymbol{X}} = \hat{\boldsymbol{f}}(t, \boldsymbol{X}), \quad \boldsymbol{X}(0) = \boldsymbol{X}_0 \tag{3.29}$$

Where:

$$\hat{\boldsymbol{M}} = \begin{bmatrix} \boldsymbol{I} & \boldsymbol{0} \\ \boldsymbol{0} & \boldsymbol{M} \end{bmatrix}, \quad \hat{\boldsymbol{f}} = \begin{bmatrix} \boldsymbol{u} \\ \boldsymbol{f} \end{bmatrix}, \quad \boldsymbol{X} = \begin{bmatrix} \boldsymbol{q} \\ \boldsymbol{u} \end{bmatrix}$$

In order to obtain a value for $\dot{X}$, it is sufficient to solve the linear system associated with Equation 3.29. The global mass matrix is symmetric: this property can be exploited to solve the linear system faster at each iteration.

The recursive formulation has allowed to describe the multibody system without the need for constraint equations. If future work will require the implementation of constraint equations, an approach based on Lagrange multipliers can be used. While this allows to easily add the constraint equations to the system's ODE, this is likely to transform the problem into a Differential Algebraic Equation, which requires dedicated strategies.

Concerning the numerical properties of the ODE, it can be observed that the generalized velocities $\boldsymbol{u}$ vary with time much more rapidly than the coordinates $\boldsymbol{q}$. Angular velocities at the joints, especially at the last elements, tend to assume high values due to the propagation of high frequency oscillations. Unless the integration step size is taken to be exceedingly small, the coordinates of the system will drift away fast from the reference solution curve. This numerical phenomenon is regarded as "stiffness" [41]. Equations which show such characteristics must be handled carefully during integration, to avoid significant drift or instabilities. This is true especially when using small damping coefficients and using a large number of elements in discretization. In fact, the high frequency modes are not eliminated and can lead to a fast deterioration in accuracy, as it can observed from original work from Fritzkowski [30]. The adoption of bending stiffness and damping limits the capability of the elements to freely rotate at the joints, effectively improving the stability properties of the system. Nevertheless, the adoption of excessive damping coefficients is prone to make the simulation unstable when an acceptable timestep is used. Further discussion will be provided in Section 4.1.5, where an analysis on the stability of the system is performed.

3.6 Software Implementation

The equations of motion for the model were computed with the aid of the software Maple [42], which allows for powerful symbolic manipulation. Using a large number of elements in the rope discretization leads to definition of many generalized coordinates to describe the system. Nevertheless, the software is able to compute derivatives of large expressions with many variables, while also providing meaningful simplifications in the expressions. The multibody system is formulated via a set of identical elements, using a recursive formulation with globally-referred angles. In this context, it was possible to find a closed-form expression for the equations of motion, as a direct function of the number of elements used in the rope discretization.

A Python implementation of the model was developed, because it allows to rapidly obtain a working prototype. In fact, it was soon possible to test the model, due to Python's flexibility and its vast selection of libraries. After the model verification, Python's limits in the speed of computation became evident. The software implementation of the model computes the equations of motion in the form:

$$\boldsymbol{x}' = \boldsymbol{f}(\boldsymbol{x}, t)$$

It is reasonable to adopt a compiling based programming language like C/C++ to solve speed issues. In fact, after compilation, the function is no longer interpreted but executed directly in machine code. However, the implementation and verification of the model in such languages would have taken considerable time from the other scopes of the analysis. Fortunately, Python available libraries are capable of solving a large number of problems. *Numba* [43] is a library which allows Just-In-Time Compilation of Python code into machine code, making use of the LLVM compiler technologies. It is best suited for numerically oriented applications, with a large use of for loops and array manipulation, like in the computation of the system's equations of motion. Numba is distinguished from other Just-In-Time compiling libraries for its easiness of use. Variables' types don't have to be explicitly defined, it is automatically handled by the Numba function decorator. Naturally, there are some limitations to its capabilities: not all Python objects and functionalities can be interpreted. However, Numba is capable of autonomously manage the *Numpy* library, which is the main founding block of Python scientific computing. Further, Numba also allows automatic parallelization of loops and heavy computations over the available CPU cores, whenever it is possible. The results allowed for a computational speedup of a factor of 20x. On top of that, for future Python based applications, one might consider using *Numbakit-Ode* to perform the integration. Numbakit-Ode is a Numba-based library which is specialized in solving ODEs fast, exploiting Numba's capabilities and speed. Additionally, it offers many possibilities for the type of solver to be used. If both tools are used at the same time, the speedup with respect to a native Python/Numpy implementation is in the order of 100x.

The rope model was imported into the In-Air-Capturing larger scale simulation, which is developed in Simulink [44]. A simple use of Matlab's API allowed to incorporate the Python code. A description of the simulation scheme is presented in Section 4.2.

4 Results

The modelling approach proposed in this thesis introduces original features compared to the work from Fritzkowski et al. [30]. As a consequence, it must go through the validation process. The verification of such a complex body model is a challenge, since it cannot be done using standard, available benchmarks. While the experimental validation is left for future work, this thesis still demonstrates the correctness of the physical model, by analyzing the energy balance of the system. Test cases will be used to show that the overall dynamics of the systems follows the intuition. The model is later tested in the IAC general simulation. A sensitivity analysis on the rope parameters is performed, to find a set of specifications which matches the requirements of the application. The response of the system to perturbations, such as the TA wake and control inputs on the ACCD, is shown.

4.1 Model Verification

Extensive testing of the proposed rope model is essential before its implementation in full-scale simulations. However, validating such systems is not a straightforward task, as there are no standard benchmarks in the literature that are well-suited for this specific application. Traditional beam benchmarks, for instance, do not offer meaningful insights into problems involving large displacements and deformations. The ideal approach to validate the model would be to utilize experimental results. This would allow for a precise comparison to verify if the dynamics and frequencies align with the actual behavior of a flexible rope. Moreover, the presented model incorporates physical parameters, such as bending stiffness and damping coefficients, which may not be readily available in material datasheets. Experimental data would enable the fine-tuning of these parameters, which are currently only estimated in this work. DLR plans to conduct the experimental phase, which is inevitable for the validation process of the IAC mission.

For the scope of this thesis, we limit ourselves to show the correctness of the physical model, by analyzing the energy balance of the system. The methodology was described in Section 3.4: variations in the mechanical energy of the system must be equal to the cumulative work performed by the generalized forces. Although this analysis does not guarantee that the model accurately describes the rope motion, it ensures that the physical model is correct and that the proposed features are reasonable [30].

Subsequently, we proceed to test the model's features in simple scenarios before proceeding to the full-scale simulation. We start by analyzing a simple rope swing and then progress to apply various external actions to the system, such as forces and rheonomous constraints. Finally, we conduct an examination of the model's sensitivity to the rope discretization and the type of integration scheme employed.

4.1.1 Rope Swing

In this test case, a rope has its top end fixed and is let swing freely. The only external force acting on the system is the rope weight. This test allows to check if the description

of the 3D dynamics is correct. In fact, the original work only covered the 2D case, so this is the first original feature introduced in this work. Initial condition for the rope state is set so that we can check if the new set of angles is modelled correctly. First node is fixed in the origin, polar angles are set to $\pi/2$, while the azimuth angles are set to $\pi/4$.
A rope with the following specifications was used:

n	L_{tot} [m]	m_{tot} [Kg]	k [N/m]	K_t [Nm^2]	c [Nms/Kg]	c_k [Ns/mKg]
30	250	80	25000	170	1	50

In this test case, a low damping coefficient will be used, resulting in a very flexible rope. In fact, the goal is to examine if the simulated dynamics resembles the intuitive behaviour expected from slender, flexible bodies. The simulation is run for 15 seconds, which allows to the rope to perform one full swing. A time step of 10^{-2} s was used, along with a standard RungeKutta ODE solver of fourth order. A 3D visualisation is displayed in Figure 4.1:

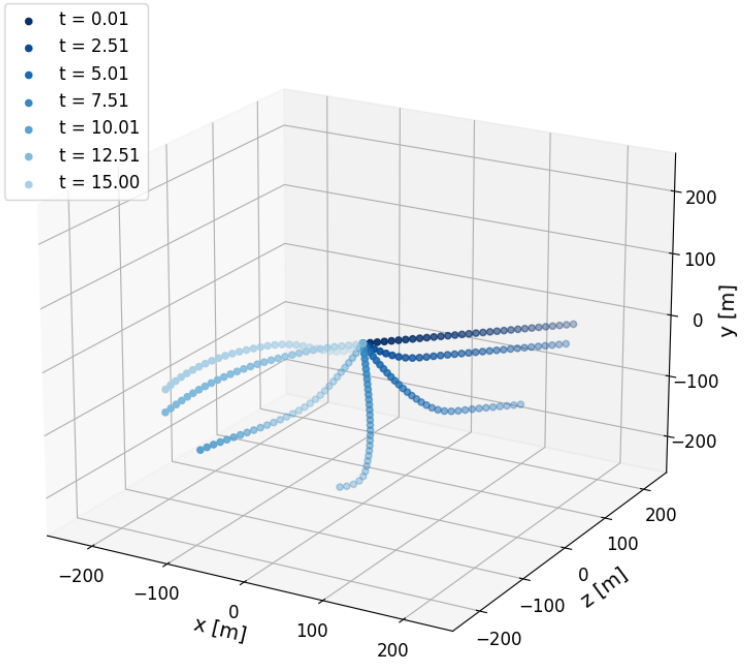

Figure 4.1: Rope simple swing under its own weight.

The rope shows oscillations which seem to match the expected behaviour. Compared to the original work [30], it is clear how the addition of damping features to the system allows to limit the chaotic dynamics of multi-pendulum models. In fact, the smoothness of the swing is associated with the damping effect incorporated at the joints.

Rope Elongation:

Figure 4.2 shows the elongation of the rope. The modelling approach for this feature was described extensively in Section 3.3.6.

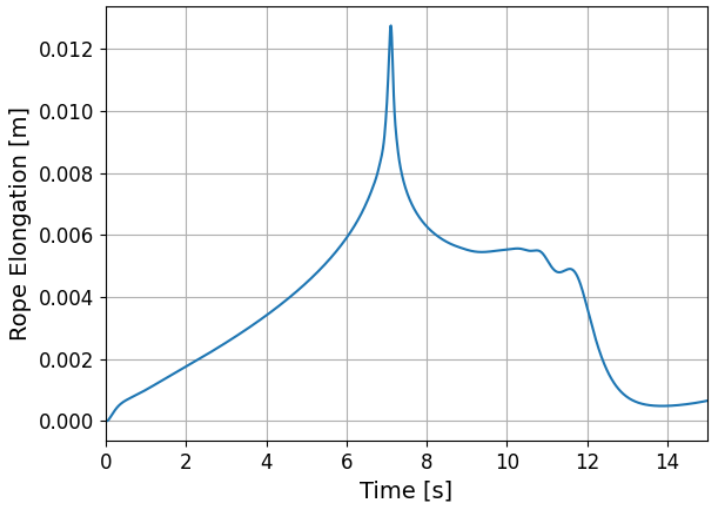

Figure 4.2: Rope elongation in the simple swing test case.

The rope starts with a null elongation, but this increases when the rope assumes a vertical configuration. As one might expect, the stress is mostly relieved at the end of the swing, where the rope finds itself with minimal velocity.

Energy Balance:

The energy balance of the system is displayed in Figure 4.3. It can be observed that the system loses mechanical energy overtime, but this is exactly equal to the work of dissipative forces, since there are no other external forces acting on the system.

It is interesting to notice that the majority of the dissipation takes place when the rope is in a vertical configuration, where the velocity assumes the maximum value. If we removed the damping out of the system, the last nodes would assume a very high angular velocity due to the propagation of the high freq oscillations through the chain of many elements. This can be observed in Fritzkowski's work [32]: the contribution of the velocity of the last nodes to the total kinetic energy is very large in this kind of configuration. This is what would ultimately lead to the failure of the simulation due to numerical instabilities, therefore the key importance of adding damping features to the system.

The difference between the mechanical energy variation and the work done by dissipative forces is minimal. It is effectively the residual error accumulated during the integration steps. A visualisation of the error is shown in Figure 4.4. This percentage shows the size of the integration error with respect to the maximum value of the mechanical energy of the system during the simulation. The integration error, during

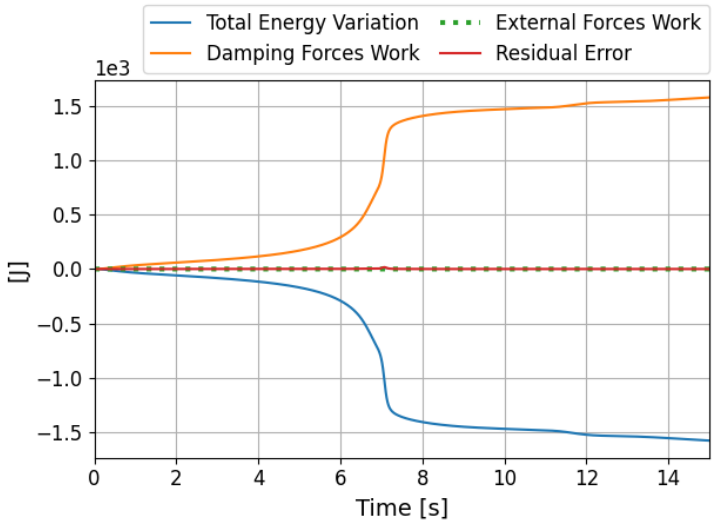

Figure 4.3: Energy balance for the system, in the simple swing test case.

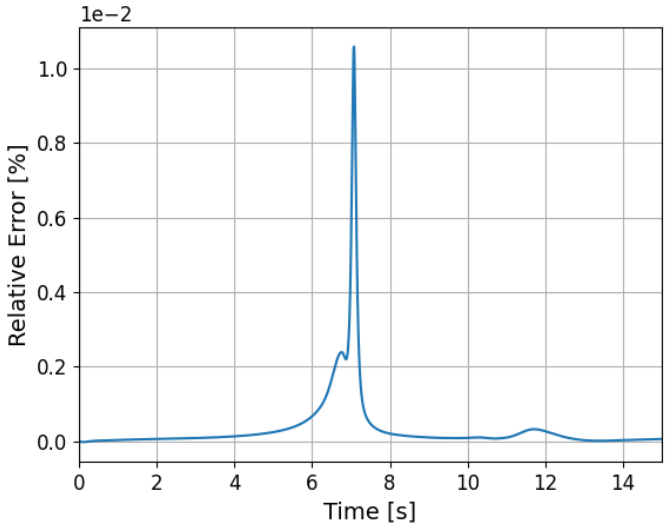

Figure 4.4: Residual error in the energy balance, in the simple swing test case.

most of the simulation, is below 0.1%. Given the relatively large time step used in the simulation, the size of the error is overall small. However, this test case does not stress the rope model with large external forces and actions. It is likely that the stability will be challenged when increasing the forces applied to the rope. This can be seen as an exploding relative error. Therefore, this kind of analysis must be performed also in later tests.

The same simulation was run with a lower time step of 10^{-3} s. The relative error is approximately ten times lower compared to the previous case. Using a lower time step also helps with the stability properties.

It should be noticed that the most critical instant, from an integration accuracy

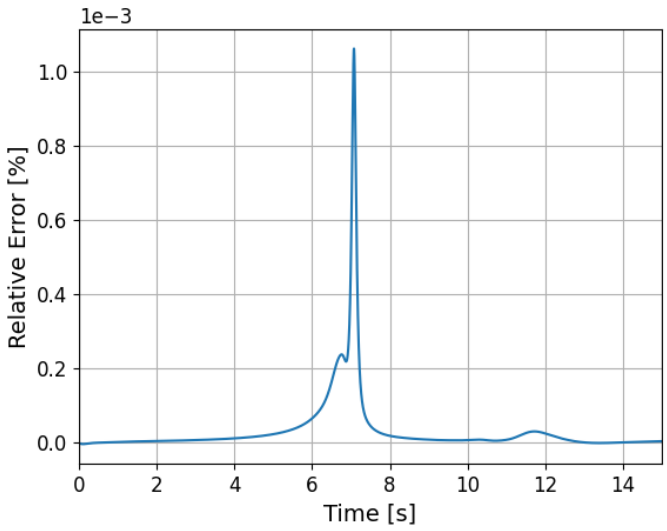

Figure 4.5: Residual error in the energy balance, but using a lower integration time step.

perspective, corresponds to the rope approaching a straight configuration with large momentum. In fact, a spike in the integration error can be observed for those time instants. In general, in these kinds of configurations, the model shows a more "stiff" behaviour. State velocities tend to change much more rapidly, compared to the state variables. The effect is more evident when many elements are used in the rope discretization: the system is more chaotic and prone to be unstable. In general, this behaviour will be further examined in later tests.

4.1.2 External Forces

Let's now transition to a test scenario more closely aligned with the IAC context. In this case, the upper end of the rope remains anchored at the origin, while a consistent external force with components (10, 0, 10) kN is exerted on the lower end. The initial polar angles are set to $\pi/4$, while the azimuth ones are set to zero. For this test case, we use a rope with stiffer specifications:

n	L_{tot} [m]	m_{tot} [Kg]	k [N/m]	K_t [Nm^2]	$c1$ [Nms/Kg]	c_k [Ns/mKg]
30	250	80	25000	300	100	50

External forces of this magnitude require a stiffer rope, otherwise the system is prone to go unstable or give unrealistic results. The Cartesian position of the rope bottom end is shown in Figure 4.6.

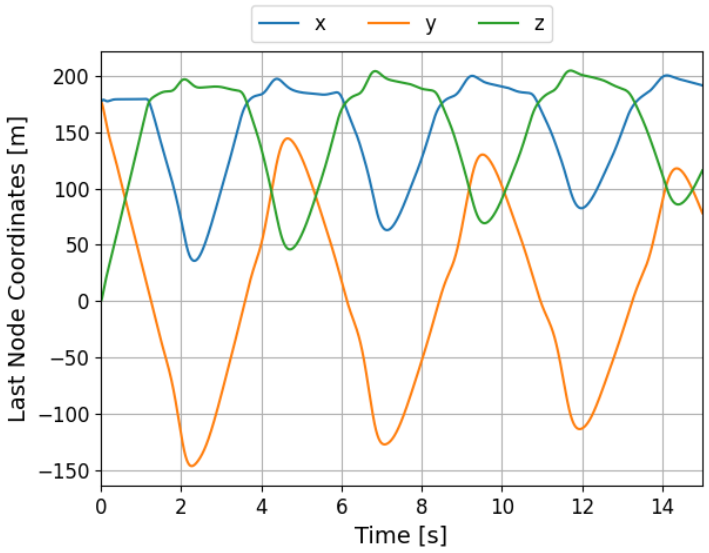

Figure 4.6: Position of the rope bottom extremity, in the external forces test case.

The external force is constant and in the same direction, so the rope continues oscillating around an equilibrium position driven by its momentum. Higher damping coefficients allow the system to start converging to a steady-state equilibrium. While damping generally allows the system to be stabler, the use large values for the coefficient also damping also increases the stiffness of the system equations. In fact, this test case was unstable with time step h= 10^{-2} s, so h= 10^{-3} was used instead. It is possible to use h= 10^{-2} as time step, but only if the rope was discretized with 20 or less elements. As it was observed in the previous test case, using many elements contributes to the stiffness of the equations, so a trade-off with damping must be done.

Rope Elongation:

Figure 4.7 shows the elongation of the rope during the simulation. The value mostly oscillates around the outcome expected by directly applying Hooke's law. However, spikes are noticeable when the rope assumes a fully straight configuration. This phenomenon arises due to those configurations possessing high momentum, and do so being mostly critical from a numerical standpoint.

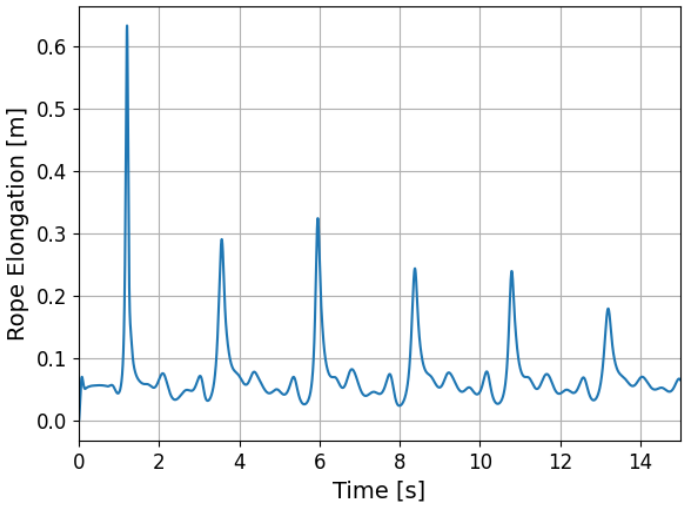

Figure 4.7: Rope elongation in the external forces test case.

Energy Balance:

The energy balance for the system can be observed in Figure 4.8. The work done by the external force drives the mechanical energy to change, but part of that energy is lost by means of the dissipative forces. The variation in mechanical energy of the system starts to converge to a constant value, because of the effect of the dissipation. Even in this case, the balance is preserved, since the residual error is close to zero.

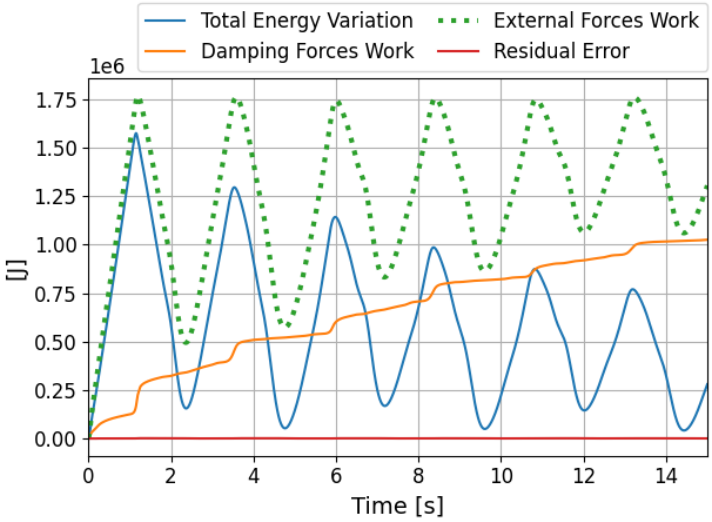

Figure 4.8: Energy balance for the system, in the external forces test case.

Figure 4.9 shows the relative violation of the conservation of energy during the simulation. Comparing it to the previous test case, it is observed that the relative error

remains of the same order of magnitude.

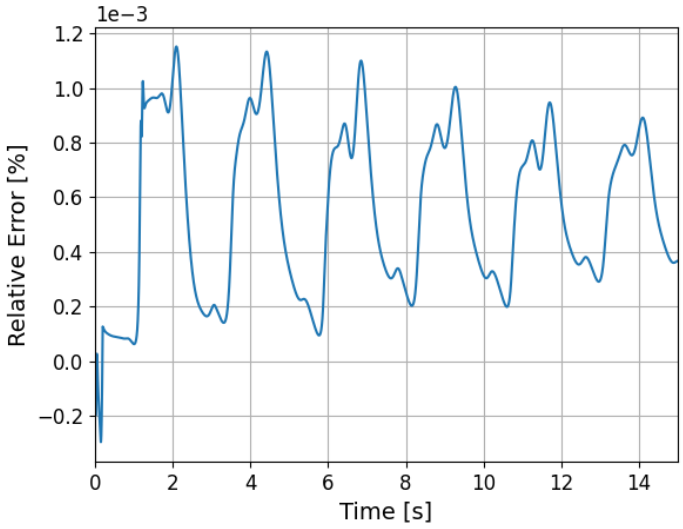

Figure 4.9: Residual error in the energy balance, in the external forces test case.

4.1.3 Rheonomous Constraints

In the following test case, we investigate the effect of rheonomous constraints applied to the upper node. Until now, it has been assumed that the rope top end was fixed in the origin. This form of constraint is classified as scleronomous, as it does not incorporate time as an explicit variable. Consequently, the equation can be expressed solely in terms of generalized coordinates [35]. We now assume that the rope upper end is attached to a horizontal moving support, whose Cartesian position directly depends on time. In this way, it is possible to test the effect of accelerations applied on the rope top node.

In the test case there are no external forces applied to the rope, except for gravity. At t=0, the rope is resting in a vertical configuration: all polar and azimuth angles are set to be zero. The motion is imposed using the following constraint function:

$$x_0(t) = \begin{cases} A\sin^2(\pi B t) & \text{for } t \leq 1/B \\ \\ 0 & \text{for } t > 1/B \end{cases}$$

with acceleration:

$$a_0(t) = \ddot{x}_0(t) = \begin{cases} AB^2\pi^2\left(\cos^2(\pi B t) - \sin^2(\pi B t)\right) & \text{for } t \leq 1/B \\ \\ 0 & \text{for } t > 1/B \end{cases}$$

The quantity $1/B$ is exactly equal to the period of oscillation: the top node will oscillate once and will stay in the origin after. Parameter A sets the amplitude of the oscillation.

If we were to manually force an oscillation at the top of the node, the intuition makes us think that we will see the propagation of the oscillation down the rope, thanks to the effect of the gravity.

The rope parameters are chosen to let the body be very flexible.

n	L_{tot} [m]	m_{tot} [Kg]	k [N/m]	K_t [Nm^2]	$c1$ [Nms/Kg]	c_k [Ns/mKg]
70	10	10	25000	1	0.01	50

A large number of elements is used: the focus is to accurately observe the oscillations propagating through the rope. The evolution of the rope is shown in Figure 4.10.

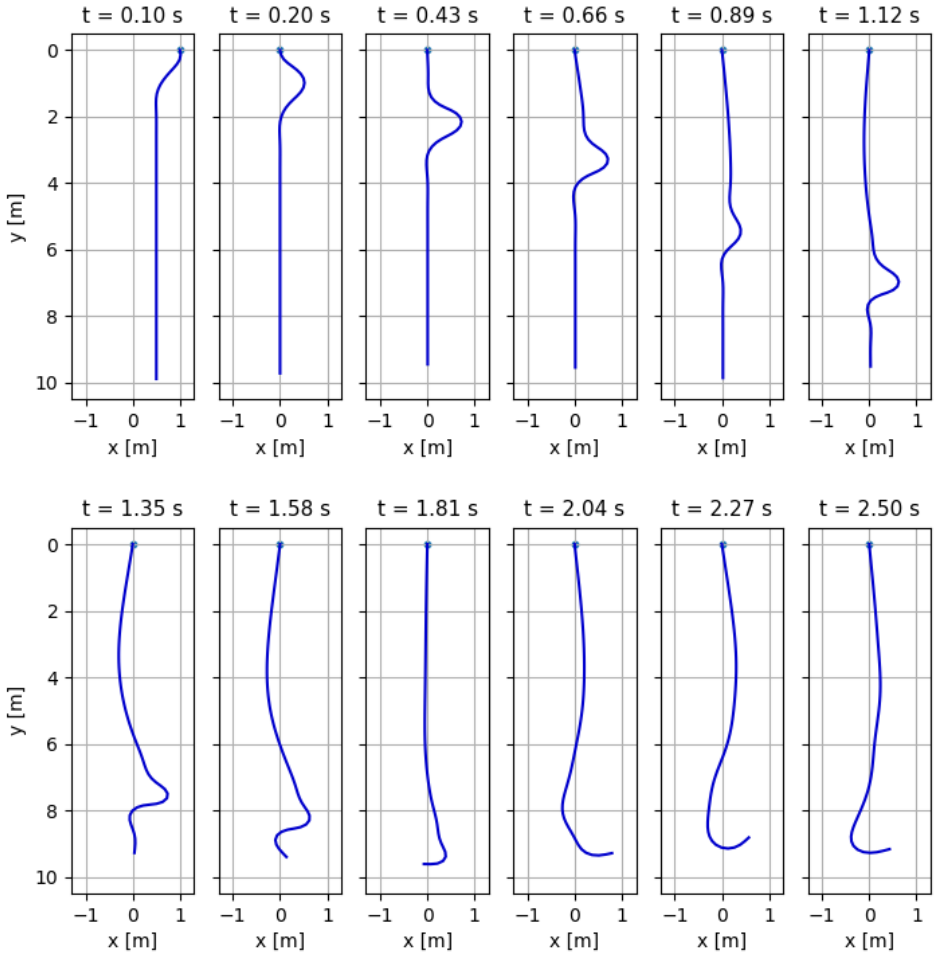

Figure 4.10: Visualisation of the rope dynamics when a motion is imposed at the top node.

The dynamics follows the intuition of the wave propagating throughout the rope. In Figure 4.11 the same simulation is run, but removing the stiffness and damping effects from the model. It is evident how introducing these features in the system allows for a

more accurate description of the real physics. In general, the simple multibody system cannot handle oscillations of higher frequency. When these reach the rope bottom end, the system goes unstable, in a similar way as the previous test cases.

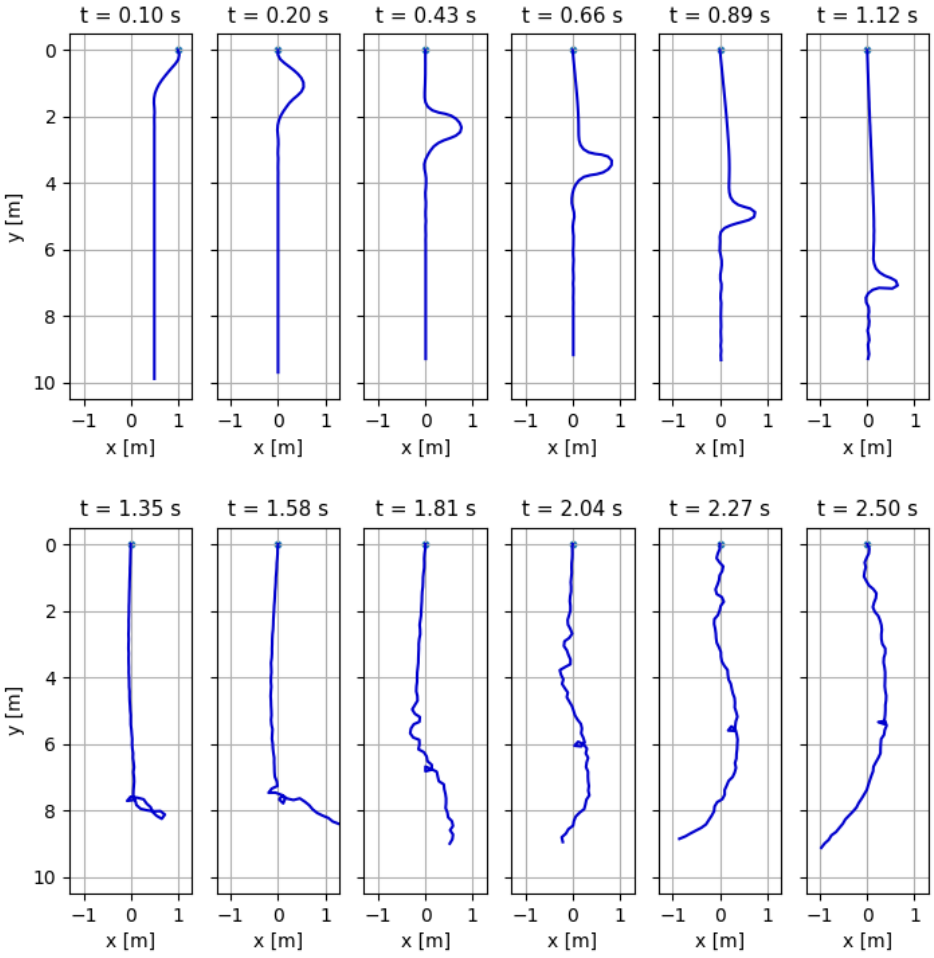

Figure 4.11: Visualisation of the rope dynamics when a motion is imposed at the top node. Bending stiffness and damping coefficients are set to zero.

This simulation could provide a solid benchmark to compare the proposed model with the dynamics of a real rope, given the simple setup and execution. Not only, one could also find accurate values for the bending stiffness and damping coefficients, through the means of the experimental validation. The same simulation will be later performed with different number of elements, to analyze if less elements can still describe oscillations with small wave length.

Figure 4.12 shows the energy balance of the system, when stiffness and damping are included. The energy introduced by the top node acceleration is computed in the same way as described in Section 4.1.2. While the balance is mostly preserved, small

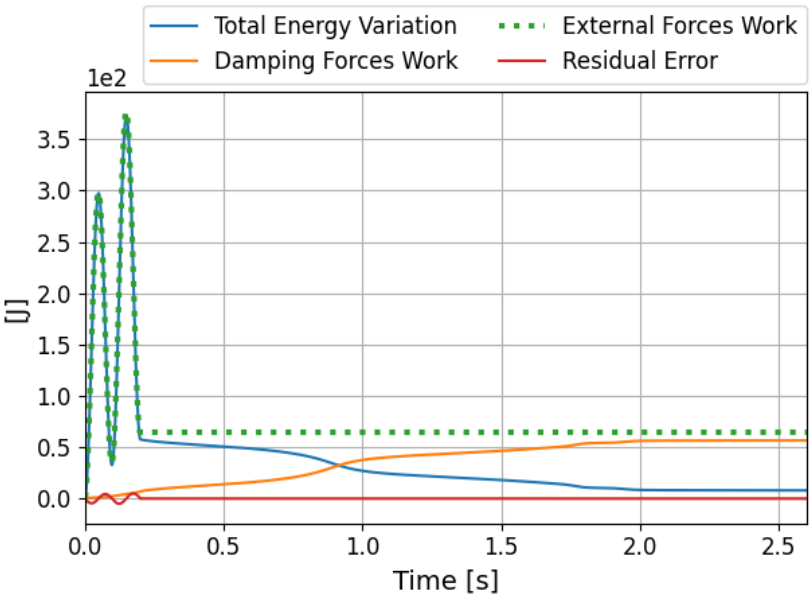

Figure 4.12: Energy balance of the system, with acceleration is applied at the top.

errors can be noticed during the imposed oscillations. The adoption of a smaller time step reduces such deviations, so they can be attributed to larger integration errors caused by the use of a continuous time law in a discrete setting.

4.1.4 Sensitivity to Rope Discretization

The overall number of elements employed in discretizing the rope holds significant importance within the analysis. The aim is to describe the dynamics of the system with good accuracy while simultaneously constraining the computational time. We explore the effect by analyzing the test cases used in Section 4.1.2 and 4.1.3, which tackle two substantially different configurations. The first one describes a very flexible rope, with an induced oscillation whose wavelength is a fraction of the rope length. The latter is a test case very close to the final application: stiff rope with high forces applied to its end. In both cases, we test with a number of elements ranging from 10 to 70.

In Figure 4.13, the results of the rheonomous test case can be observed. The same rope specifications are used, but with different discretization. It is evident how 10 elements fail to adequately capture the oscillations generated by the applied motion. The overall dynamics exhibit notable differences due to the insufficient degrees of freedom, preventing the portrayal of oscillations characterized by shorter wavelengths and smaller amplitudes. By increasing the element count, a significantly more intuitive behavior comes to light. Employing a finer mesh in the discretization process should, in theory, lead the system to converge towards the real dynamics of the rope. However, this assumption needs to be validated through experimental verification. While this hypothesis is rational, it is likely that the stability of the model will be affected by employing a vast number of elements.

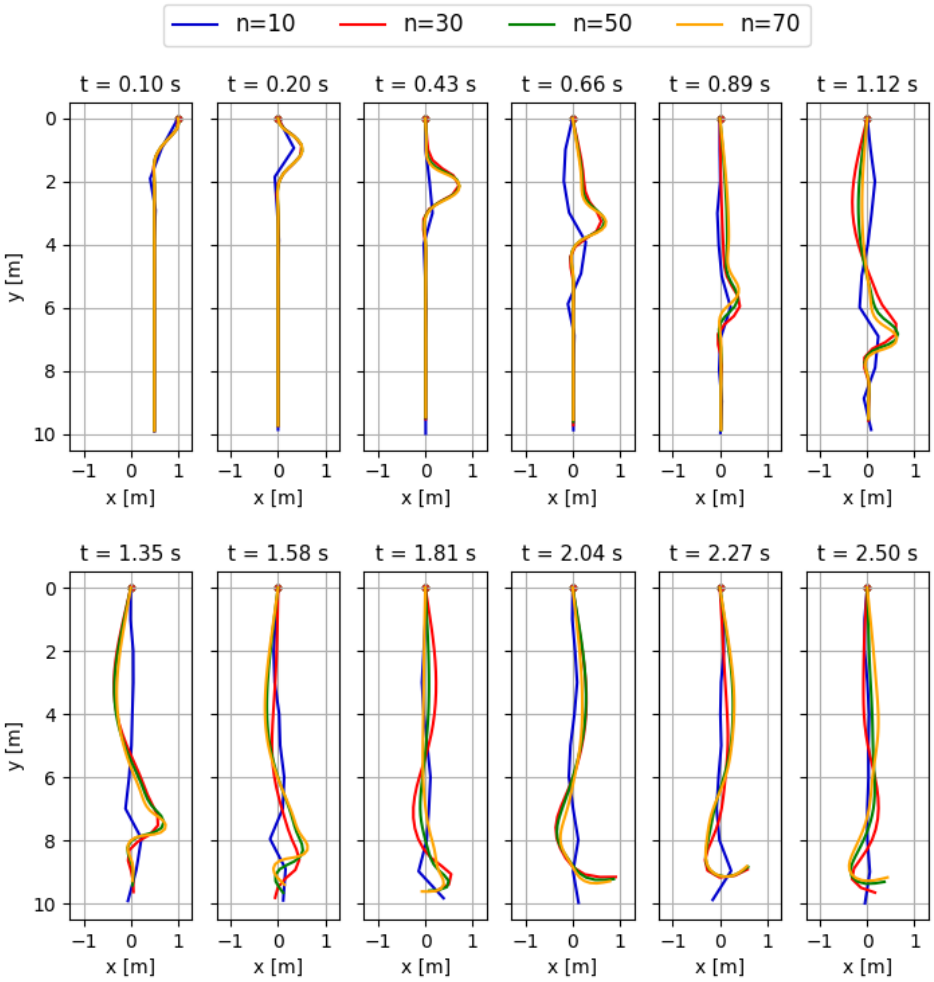

Figure 4.13: Rope dynamics when a motion is imposed at the top node, for different number of elements in the discretization.

It has been demonstrated that employing a finer discretization is essential for accurately representing oscillations of higher frequencies. However, the rope that will be used in the full-scale IAC simulations will be much stiffer than the one of the present test case. Most importantly, high forces will also be applied to the rope end, maintaining the body mostly in a straight configuration. Consequently, a large number of elements isn't necessary to describe the operational conditions.

In general, using a mesh of 30 elements seems already able to capture the most important oscillating modes, while also keeping a good estimate on the position of the final element. Despite the increased stiffness of the rope in the IAC application, its considerable length of over 100 meters justifies the use of numerous elements in the discretization process.

Figure 4.14 illustrates the impact of rope discretization in the 'External Forces' test case. This configuration closely resembles the eventual application, featuring a more

rigid rope subjected to substantial forces at its end. Consequently, it is possible to determine an appropriate discretization that can effectively depict the overall movement while maintaining a reasonable computational load.

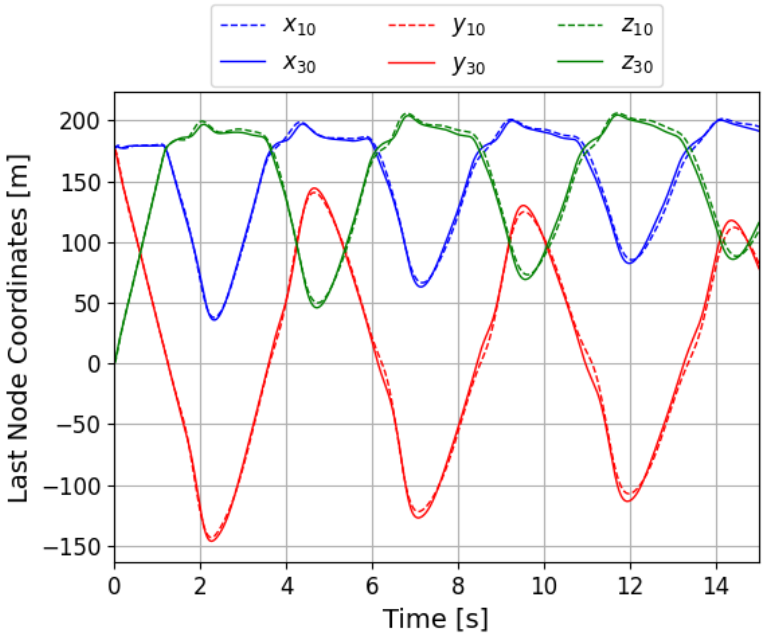

Figure 4.14: Position of the rope bottom end, under external forces and with different discretization.

Utilizing 50 elements or more within the rope mesh triggers instabilities in the simulation. This phenomenon arises from the utilization of large damping values in the rope specifications, amplifying the stiffness of the equations. If the time step is set to a smaller value, such as h = 10^{-4} s, the simulation would remain stable. Generally, it can be postulated that once a certain threshold for the discretization hyperparameter is surpassed, assuming other specifications remain constant, the system's stability is compromised.

Analyzing the results from Figure 4.14, it becomes evident that the different discretizations yield relatively comparable results. In contrast to the preceding test case, 10 elements appear capable of describing a very similar motion for the rope lower end. In scenarios involving rigid ropes and large, applied forces, it can be inferred that opting for a lower discretization does not result in significant accuracy loss. This can be attributed to the configuration's dynamics approaching that of a beam. With concentrated forces acting at a single point, other contributions become marginal. In essence, the rope assumes an almost straight configuration, rendering a fine discretization unnecessary. Similar conclusions will be drawn in the IAC full-scale simulation results section.

Generally, this indicates that when the rope is not slack, a high discretization level is not needed. It is reasonable to explore in future work the use of an adaptive number of elements, depending on the rope overall curvature.

4.1.5 Choice of ODE Solver

As mentioned in the previous sections, the final set of ODEs manifests the phenomenon of stiffness for certain configurations. While high damping coefficients and finer rope discretization are often necessary to describe a natural dynamics, they both affect the stability of the system. Adopting a low time step is generally sufficient to avoid instabilities, but it compromises the computational efficiency requirement. The type of ODE solver used in the simulation is likely to play a key role in guaranteeing stability properties.
ODE integrators can be divided in explicit and implicit ones, depending on the type of information they use to compute the new state [41]. Explicit methods compute the new values y_{i+1} directly from the current state y_i. Implicit ones, instead, require to solve an equation involving both the current state and the later one, to estimate the latter y_{i+1}. Consequently, implicit methods require heavier computation compared to explicit schemes. Nevertheless, they exhibit superior stability when dealing with stiff problems, allowing the adoption of a larger step size. In addition, ODE solvers can also be classified in terms of their order, which generally reflects the level of accuracy of the method.

The aim of this section is to explore different types of ODE solvers, investigating whether they are able to keep the simulation stable with the defined step of $h = 10^{-2}$. Finally, a trade-off with their computing efficiency will be performed. Driven by these motivations, we run the 'External Forces' test case with different specifications and with different numerical algorithms. The ODE solvers that will be tested are the explicit RungeKutta4 and Dormand-Prince (RK8) methods, and the implicit Backwards Difference Formula method of second order (BDF2). The general aim is to examine whether implicit integrators show to be stabler than explicit ones. However, given the higher computational burden of implicit schemes, it is also useful to check if higher order explicit integrators are sufficient to solve numerical instability problems. Additionally, different step sizes will be used, both the required $h = 10^{-2}$ and a lower one $h = 10^{-3}$. The values of the damping factor c and the number of elements n have shown to affect the stability of the system. Consequently, they will be the rope parameters of the analysis. Table 1 reports the results of the simulations for all combinations of the parameters and solvers. For each simulation, it is only reported if the simulation has stopped early due to instabilities. As it can be observed, the BDF2

Solver:	RungeKutta4		Dormand-Prince		BDF2	
h:	10^{-2} s	10^{-3} s	10^{-2} s	10^{-3} s	10^{-2} s	10^{-3} s
c = 10, n= 20:	✓	✓	✓	✓	✓	✓
c = 10, n= 30:	✗	✓	✓	✓	✓	✓
c = 100, n= 20:	✗	✓	✓	✓	✓	✓
c = 100, n= 30:	✗	✗	✗	✓	✓	✓

Table 1: Stability of the simulation with different solvers, time steps, and rope parameters.

remains stable in all the configurations of the parameters that were tested. On the

contrary, explicit methods struggle to remain stable for larger number of elements or larger damping coefficients. Using a higher order explicit solver partially solves the stability issues, but only for a limited region of parameters.

In general, it is recommended to use implicit methods to solve the equations of the model. However, this category of methods requires the solution of an equation to obtain the state variables at the next step. Numerical algorithms to solve equations, such as the common Newton-Rapson method, make use of the function derivative to estimate the solution of the equation in the form $f(x) = 0$. This cannot be applied to our model, since the derivative of Equation 3.6 cannot be computed analytically, because of the complex form of the equations of motion. One must resort to other kinds of methods, such as the secant method, which does not make use of derivatives, but is definitely less efficient in terms of speed of convergence. The procedure of implicit methods, in general, is slower than explicit methods, especially for systems like the proposed rope model. In fact, the initial value problem is rather convoluted, with every function evaluation being rather expensive. Given the absolute superiority of implicit methods in the integration of the ODE, further work shall be done to seek an efficient implementation for our system.

4.2 IAC Simulation

The rope model is now tested in the larger scale IAC simulation. A lumped mass, equivalent to the total mass of the ACCD, is added at the end of the rope. In such manner, the additional inertia is taken into account inside the rope equations of motion. Methodology is described in Appendix A. Figure 4.15 briefly describes the scheme of the rope sub-module that is input to the simulation. The rope model is essentially a function that computes the equations of motion, in the form of $\dot{\boldsymbol{X}} = \boldsymbol{f}(\boldsymbol{X})$. The EOM system block requires a set of inputs:

- The TA acceleration. As explained in Section 3, the model describes the relative motion of the rope with respect to the TA, since the rope shares the top node with the aircraft. Accelerations in the TA motion will generate apparent forces, due to the reference frame being no longer inertial. For this reason, the Cartesian coordinates of the TA acceleration must be input to the model.

- External forces applied to the rope. These can be of two forms: distributed along the rope or lumped, applied in a specific rope element. In the context of application, lumped forces are only applied to the end of the rope, in the connection point with the ACCD. Distributed forces can be generic, with only gravity being present in this environment. Drag and lift have a custom formulation, so they are handled directly in the model.

- Rope specifications. These can be directly fixed in the EOM block, but it's useful to keep it separate for parameter sensitivity analysis and for description of the deployment dynamics in future work.

The EOM system block outputs the derivative of the state, which is fed to an ODE solver. Initial conditions for the system, in the form of rope angles and elongation, are

provided. In this application, the initial rope configuration will be set to be straight and horizontal with respect to the plane. Fixing the rope length and its bottom end position, one can easily obtain the rope polar and azimuth angles which produce that configuration. This is reasonable since it will be very close to the steady-state condition. In other fields of application, where the rope is slack, these initial conditions might not describe a realistic scenario. As such, it is necessary to solve the inverse kinematics problem to find a stable initial condition. Closed form solution for the initial condition problem exist in the catenary equations [45], which describe the natural curve of an hanging rope.

The new rope state is used to compute the position, velocity and acceleration of the end node of the rope. This will be fed to the capturing device dynamics, effectively imposing the kinematics of the ACCD top point. The two systems are now coupled, constrained to share one point at the interface. Only the translational motion of the ACCD is defined by the rope, since torsional effects are not considered for the time being. In fact, the rotational motion of the ACCD was modelled separately, outside of the rope model.

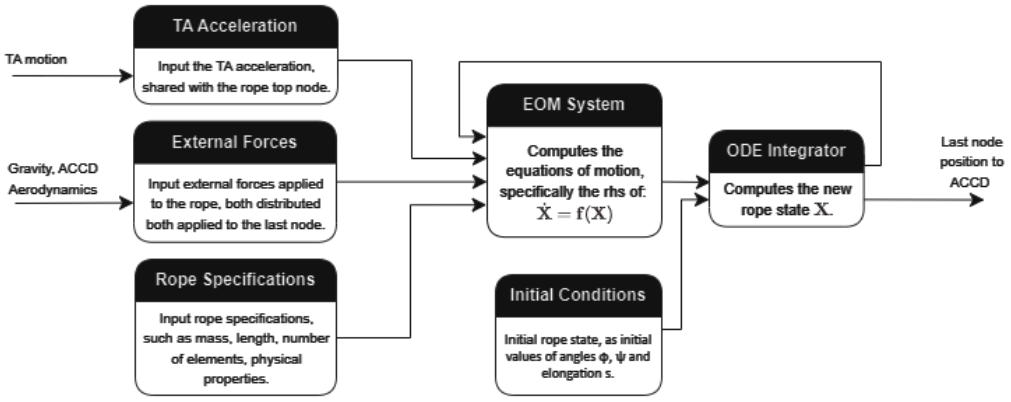

Figure 4.15: Scheme of the simulation environment.

The scope of this analysis is to test the rope model when incorporated in the larger scale simulation. The simulations will be performed in cruise flight conditions for the TA. First, the key requirements of the IAC manoeuvre are discussed. Then, an extensive sensitivity analysis on the rope parameters is performed, to propose a final set of rope specifications that fit the requirements of the application. The first simulation will cover the most critical scenario from a stress perspective, specifically when the RLV is connected to the ACCD. This will suggest the required rope breaking strength and stiffness. Following, we study the maneuverability of the ACCD for a number of rope parameters and environmental conditions. The aim is to find a set of specifications which allows agile maneuvers for the capturing system, while also achieving stability in reasonable time frame. In the first simulations, we will simply release the capturing system from a completely horizontal position with respect to the aircraft. A later step is to give the ACCD a set of open-loop control commands,

to check the response and the maneuverability for different rope parameters. The different command inputs applied to the ACCD are shown in Figure 4.16.

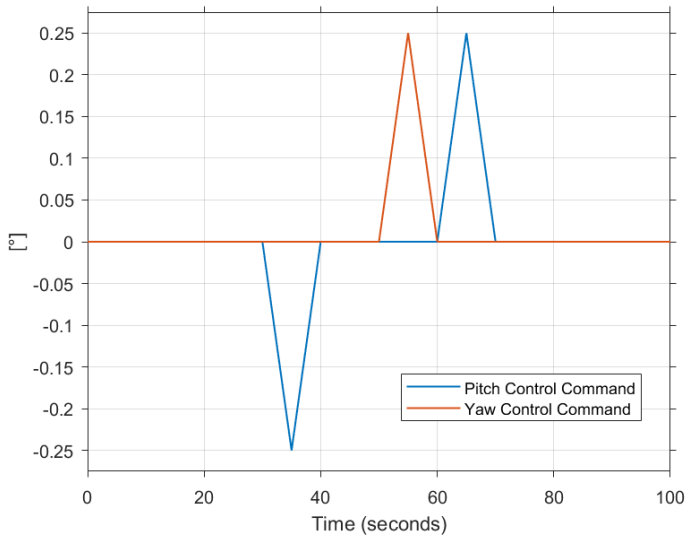

Figure 4.16: Control input to the ACCD angles.

Control commands set the ACCD fins deflections, which will then affect the ACCD overall pitch and yaw angles. The mapping from the desired ACCD angle to the command in flap deflection is left implicit, but it is accurately described in the work [46]. The four fins of the ACCD can assume a vast number of configurations. Some simplifications, based on a superposition approach, have been made to easily translate the contributions of each fin to the aerodynamic actions. A behaviour close to the reference signal will be actually observed in the ACCD angle of attack and side-slip angle. In fact, these angles are measured in the ACCD aerodynamic frame, which is relative with respect to the airflow. Further details can be found in the aforementioned work.

Following, the analysis focus on the effect of the TA wake. This is essentially a perturbation to the free stream velocity in space, so it might heavily affect the maneuverability of the ACCD. Not only, its turbulent nature might potentially affect the stability of the system.

A final element of analysis is the choice of the rope discretization. In the same way as in the test cases, the aim to find a proper computation-accuracy trade-off.

4.2.1 Requirements

The feasibility of the IAC capturing phase imposes a set of technical requirements. The objective of this Section involves determining rope parameters that can successfully meet these requirements.

- The ACCD shall be as maneuverable as possible, allowing for a fast repositioning in space during the capturing process. This can be examined by looking at the ACCD position in space overtime.

- The simulation shall be efficient from a computational efficiency perspective. The global time step is set to h= 10^{-2} s. As a consequence, the parameters that affect the computational load are the number of elements in the rope discretization and the type of integration scheme. Trade-offs must always be performed by also considering the accuracy and stability requirements.

- The ACCD shall lie below the wake zone (up to 30-40 m). Previous study [7] has shown that control strategies struggle to make the ACCD controllable in the region affected by the wake.

- The rope must be able to sustain the loads coming from the capturing device, and later from the rocket first stage. It must mentioned that both the ACCD and the RLV are winged, meaning that they are able to generate substantial lift forces. As such, a large share of the weight of the two systems will be counterbalanced by the aerodynamic forces. At this stage of the simulation, the main loads applied to the rope will be the drag forces of the bodies attached to its end.

- The capturing system must be in principle stable on its own, without the necessity of control inputs to the ACCD. In other words, the system shall recover autonomously from disturbances in pitch, yaw, roll angles. This property is called *aerodynamic stability*. The ACCD is designed to possess such characteristics, the aim is to verify that the rope does not affect it. Additionally, it is also of great importance that the capturing system converges fast to a stable position, so that is possible to perform multiple capturing attempts in the given window.

4.2.2 Choice of Rope Specifications

The choice of an optimal set of rope specifications is not a trivial task, due to it being a multivariate optimization problem. While there are standard ways to tackle it in the literature, the computational effort of running the simulation requires to divide the problem in steps. Generally, the aim of this work is to propose suitable rope specifications for this application. An in-depth optimization can be performed in future work.

Hereafter the key rope parameters will be listed, along with their main influences on the rope dynamics.

- **E** is the Young Modulus, measured in GPa. It is an intrinsic property of the material, and affects the stiffness of the rope.

- **d** is the rope diameter, measured in meters. It will set the cross-section area, the area moment of inertia I, and the material mass per unit length.

- $\boldsymbol{L_{tot}}$ is the rope length, measured in meters. Its value affect the rope mass and stiffness. Longer ropes allow for larger oscillations of the ACCD position.

- $\boldsymbol{k_a}$ is the axial stiffness coefficient, measured in N/m. It can be computed from the other parameters as:
$$k = \frac{EA}{L_{tot}}$$
- $\boldsymbol{K_t}$ is bending stiffness coefficient, measured in Nm^2. Its values is calculated from:
$$K_t = \frac{EI}{L},$$
where L is the length of a single rope segment.
- $\boldsymbol{T_{max}}$ is the rope breaking strength, expressed in kN. Its value is directly obtained from the technical datasheets, and it is a function of the rope material and diameter.
- $\boldsymbol{c}$ and $\boldsymbol{c_k}$ are the damping coefficients, respectively at the joints and at the linear spring. Their values are not available in technical documentations. In this section we will use: $c = 10$ and $c_k = 50$. Proper, accurate values can be estimated during the experimental validation of the model.

The first specification to be set is the rope breaking strength. It is crucial to guarantee that the rope is able to sustain the loads in the most critical configuration of the mission. This occurs when the RLV is connected to the capturing system, while the airplane's engines are providing maximum thrust. After having set the failure characteristics, it is possible to move forward with choosing a fitting material for the application. Suitable rope diameter and length are proposed, mostly by analyzing the effect they have on the ACCD maneuverability. The tests are repeated for different environment settings. First, the convergence of the ACCD is studied, starting from the reference horizontal configuration. Following, sample control inputs to the ACCD are enabled, to check the system's response in terms of stability and repositioning.

Max Stress:

The most critical scenario for the rope consists in the RLV connected to the rope-ACCD system, with the TA engines generating maximum thrust, while in the minimum drag configuration. The TA is considered to be the long-range jetliner A340-600 with four engines [47]. Each of these engines is expected to provide a maximum thrust of 260 kN when at sea level. At the same time, the RLV is the first stage of a 3-Stage-To-Orbit rocket concept [48], with a mass of approximately 80 tons. The launch vehicle is added to the model in the same way as the ACCD, so as a lumped mass attached to the end of the rope. This is an extreme simplification, but it reasonable for the only purpose of computing the max axial stress. Drag of the RLV is approximated to 50 kN, while the lift is supposed to balance the RLV weight.

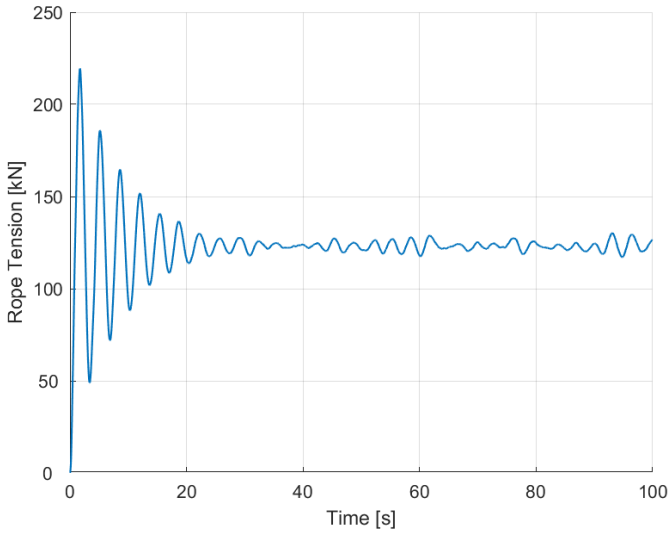

Figure 4.17: Rope tension in the most critical scenario.

Figure 4.17 shows the rope tension in the most critical scenario. In steady-state conditions, the stress oscillates around 125 kN, while it surpasses 200 kN before settling, due to inertia forces being in play. It must be reminded that the model makes use of a simplifies spring model to calculate the elongation, and the related tension. While it does not pretend to be a accurate description of the axial deformation, this model still provides good estimates when the rope is in a straight configuration, which is the case of this analysis. The field of application requires the use of high safety factors in the structure design, to take into account unexpected and extreme situations. A proper estimate of this coefficient requires a dedicated analysis, which will be left for future stages of the IAC validation. For the time being, we will require the final rope to be able to handle load which are at least four times greater than the value found in the maximum stress simulation. In later steps of the present analysis, only ropes with breaking strength greater than 500 kN will be considered.

The model with the RLV connected as a lumped mass is a substantial simplification, which can only be performed to analyze the most critical scenario. From this point on, the single capturing device will be attached to the rope bottom end. For the current stage of the simulation, it is key to understand the maneuverability of the capturing device.

Rope Material and Diameter:

The application requires materials with high performances. The focus mainly falls on the two types of rope materials: polyester and steel. Concerning polyester ones, UHMWPE ropes [49] have proven to show best performances under many perspectives. They exhibit the best strength-weigth ratios, while also guaranteeing resistance to fatigue and many chemical agents. While other ropes are cheaper, they are outclassed from most perspectives. Nevertheless, an investigation into the potential use of steel ropes was performed. Despite exhibiting inferior performance, they are considerably

heavier compared to conventional fiber ropes. It is precisely due to this weight that they could be fitting for the mission's requirements. In fact, a heavier rope would probably settle outside of the aircraft wake region. Nonetheless, due to their lower strength, these ropes would necessitate a larger diameter compared to wire ropes. This might lead to an excessive weight and stiffness. Ultimately, a trade-off must be reached.

For the UHMWPE ropes:

Diameter [mm]	Mass per unit length [Kg/m]	Breaking Strength [kN]
16	0.156	280
24	0.329	550
32	0.555	900

The displacement of the ACCD in the vertical direction, using a UHMWPE rope, is shown in Figure 4.18.

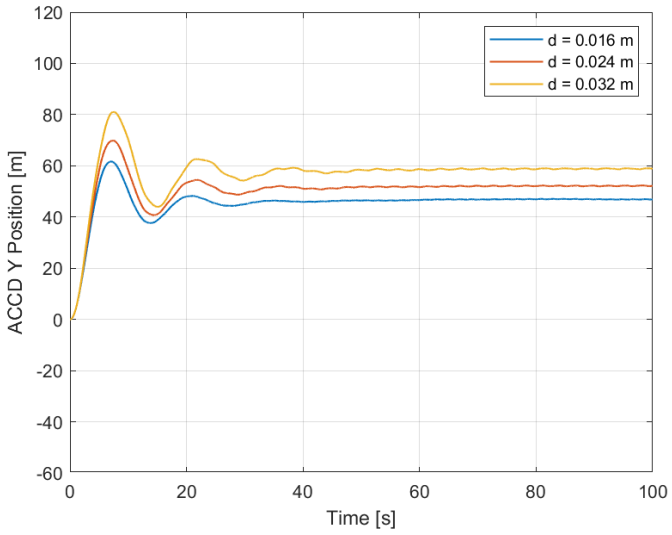

Figure 4.18: ACCD vertical position in cruise flight, using different UHMWPE ropes (L=250 m).

Initially, the ACCD is oriented horizontally to align with the aircraft, meaning it starts from a zero Y position. Rope length is set to be 250 meters. The aerodynamic stability of the ACCD is preserved, as the system quickly converges toward a steady-state position. Larger diameters lead to oscillations with a similar period, but with slightly greater amplitude. This behaviour will be observed also in later stages of the analysis, when the length of the rope is changed. In general, increasing the mass of the rope causes the ACCD to settle at a lower point, but at the cost of larger swings in the repositioning. A rope diameter of 24mm is capable of sustaining the maximum loads estimated in the previous section, while also allowing to find a stable position outside of the wake region.

The specifications for the steel ropes are hereby reported [50]:

Diameter [mm]	Mass per unit length [Kg/m]	Breaking Strength [kN]
24	2.34	375
32	4.1	645

The same simulation is run using a steel wire rope (Figure 4.19).

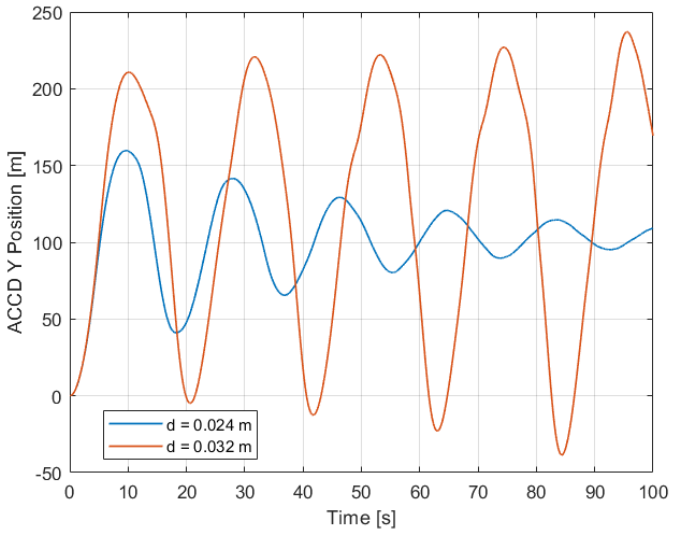

Figure 4.19: ACCD vertical position in cruise flight, using different steel wire ropes (L=250 m).

As evident from the observations, the capturing device would settle lower than 100 meters from the aircraft's horizontal reference direction. This outcome arises due to the rope's significantly greater mass, nearly ten times that of UHMWPE ropes of identical diameter. While this ensures a considerable distance from the wake region, it comes at the expense of exceedingly substantial oscillations. Opting for a 0.024 m diameter leads to extended oscillation damping times, because the rope inertia becomes dominant. Enlarging the diameter even further compromises the overall aerodynamic stability of the system. It is evident that steel wire ropes fail to meet the agility prerequisites, making UHMWPE ropes the preferred choice.

Rope Length:

The length of the rope significantly influences the dynamics of the ACCD. When the rope is almost straight, it effectively constraints the ACCD to maintain a fixed distance from the towing aircraft. Consequently, longer ropes allow for larger repositioning in space for the same angular movement. Moreover, longer ropes result in increased mass of the system.

The objective of this study is to determine an appropriate rope length that enables the ACCD to converge to a sufficiently low vertical position, with reasonable amplitude

in the oscillations. To achieve this, the system's response is tested by applying control inputs to the ACCD, as shown earlier in Fig. 4.16.

Figures 4.20 and 4.21 respectively show the vertical position and the sideslip of the capturing device, when the simulation is run for multiple rope lengths, with a fixed diameter of 0.024 m.

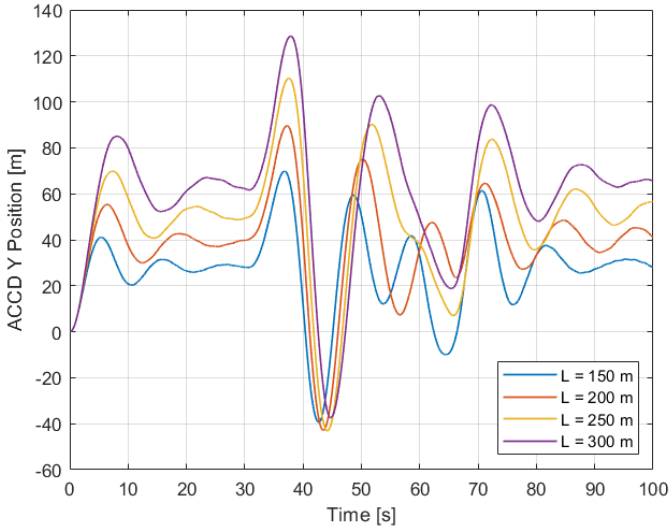

Figure 4.20: ACCD vertical position with command inputs, using different rope lengths.

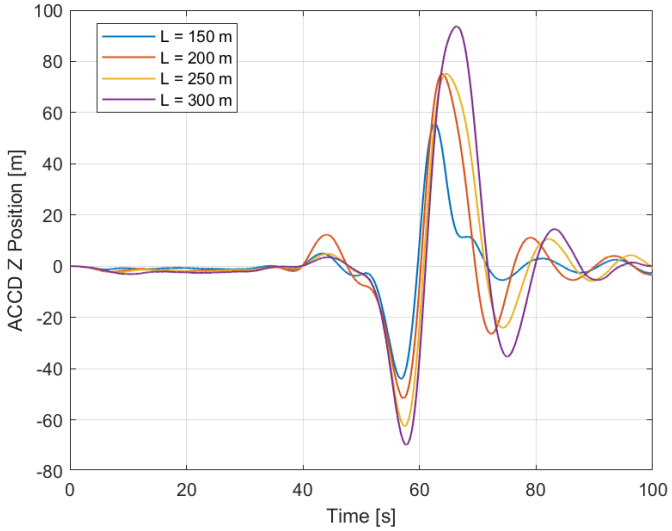

Figure 4.21: ACCD side-slip with command inputs, using different rope lengths.

The results indicate that all tested rope length values maintain the stability of the capturing device, with no configurations leading to unreasonable maneuvers of the

ACCD. Longer ropes exhibit greater displacement potential with the same control input, which may be advantageous for the IAC mission. However, longer ropes are associated with larger amplitude and longer oscillation periods, potentially having a heavy impact on the the repositioning time. The window for the capturing phase is estimated to be around three minutes [2]. Considering the limited capturing phase window, shorter repositioning times are preferred as they may allow for multiple capture attempts within the given time frame. Shorter ropes may offer a faster cycle, despite reduced movement capabilities. On the other hand, longer ropes achieve greater displacements, at the cost of larger oscillations around the stable positions. These considerations suggest that an intermediate rope length could allow an appropriate trade-off.
Nevertheless, the final determination of the optimal rope length will be made after analyzing the effects of the aircraft wake on the capturing system.

4.2.3 Sensitivity to Rope Discretization

As described in Section 3, the rope is discretized in sub-elements. A finer mesh enhances the accuracy of representing the rope's movement, particularly concerning the position of the ACCD at the end of the rope. However, this refinement results in a larger set of variables, subsequently increasing the computational load. In this context, the objective of the parametric analysis is to determine an appropriate value for n where further increments will not significantly improve accuracy. Moreover, employing a larger number of elements has demonstrated the tendency to result in stiffer equations.

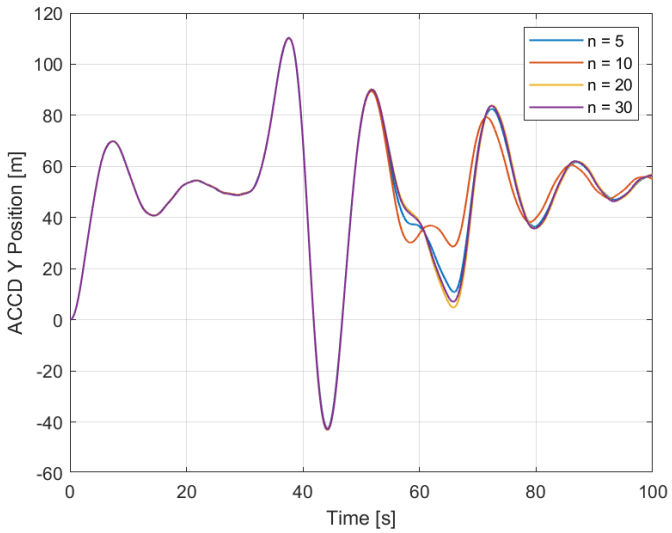

Figure 4.22: ACCD vertical position with command inputs, with different rope discretization.

In general, as it can be observed from Figure 4.22, the different rope discretization appears to have a little effect in the overall behaviour of the system.

This confirms the observation made in Section 4.1.4: when the rope is primarily straight and subjected to high forces, using only a few elements in the discretization does not significantly compromise accuracy. Even with n set to 5, reasonably accurate estimates are obtained. Beyond $n = 20$, there appears to be no discernible difference. Consequently, for this phase of the IAC simulation, a number of elements equal to 20 (or more) can offer a proper trade-off between accuracy and computational efficiency.

The majority of the forces are concentrated at the end, which is why even a few elements are sufficient. The middle elements describe the catenary curve resulting from these forces, while the end position remains relatively stable. It should be noted that the applied control input is smooth, taking approximately 10 seconds to complete the ramp. Using a more dynamic control input for the ACCD would likely result in discrepancies with different values of n.

4.2.4 Effect of Aircraft Wake

Lastly, the effect of the towing aircraft wake is analyzed. Wake turbulence is a source of disturbance that is generated as an aircraft passes through the air. As the capturing

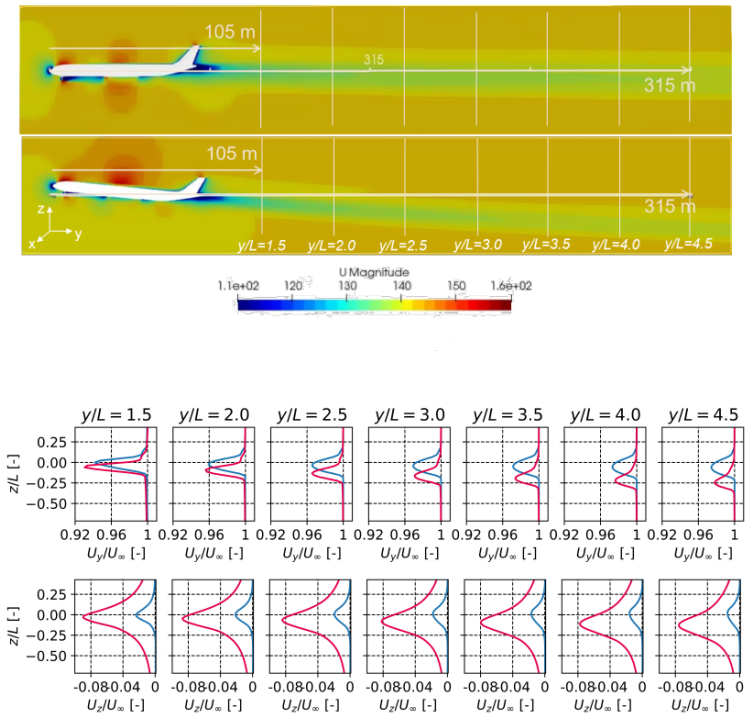

Figure 4.23: Wake profiles, in terms of variation of airstream velocity (Source: [2]).

system is deployed from the towing aircraft and follows its trajectory, it may potentially operate within the wake region.

Therefore, simulating the effect of the wake is essential, as it can impact the stability and maneuverability of the system. As it was observed, longer and heavier ropes tend to settle at a lower vertical position. While it is safer and preferable to avoid the critical wake region entirely, it is also valuable to investigate its actual impact

on the capturing system. Shorter ropes settle closer to the aircraft position, offering their own advantages. Thus, if it is determined that the wake effect is not excessively problematic, shorter ropes may be considered. Essentially, the wake changes the velocity of the relative airflow, depending on the location in space. A visualization of such effect can be observed in Figure 4.23, taken from Singh et al's work [2].

For practical implementation, it is considered that the wake becomes negligible after 50 meters. Hence, capturing systems settling below this threshold are considered to be minimally affected by the wake. The effect of the wake is tested for TA angle of attack equal to 6°, which represents the most critical scenario.

However, it is important to note that this analysis was conducted in an open-loop system, where there is no active controller attempting to guide the ACCD along the reference signal. In closed-loop simulations, the controlling strategy may encounter challenges. As the wake effect varies with position, a controller lacking robustness in this regard may lead to instability. This aspect is demonstrated in another study by Singh [7].

Figure 4.24 displays the vertical position of the capturing device as it settles freely with wake influence. As it is evident from the results, a longer rope, such as the

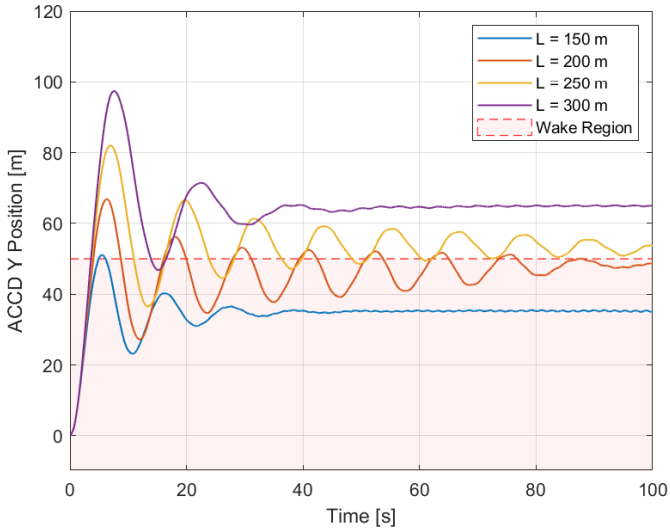

Figure 4.24: ACCD vertical position with aircraft wake and no control inputs.

300 m one, settles at a lower position with respect to the wake region. In previous simulations, it was demonstrated that 250 m ropes settle just below 50 m, where the wake has minimal impact. However, with such values, the ACCD would oscillate in and out of the wake region during convergence to a steady position. Consequently, the ACCD's position would exhibit longer oscillations before reaching an equilibrium. To avoid this behaviour, a 300 m rope is preferred.

Figure 4.25 illustrates the same simulation but with control inputs actively applied. In this scenario as well, opting for a longer rope helps in avoiding the wake region as much as possible, thus reducing unnecessary oscillations.

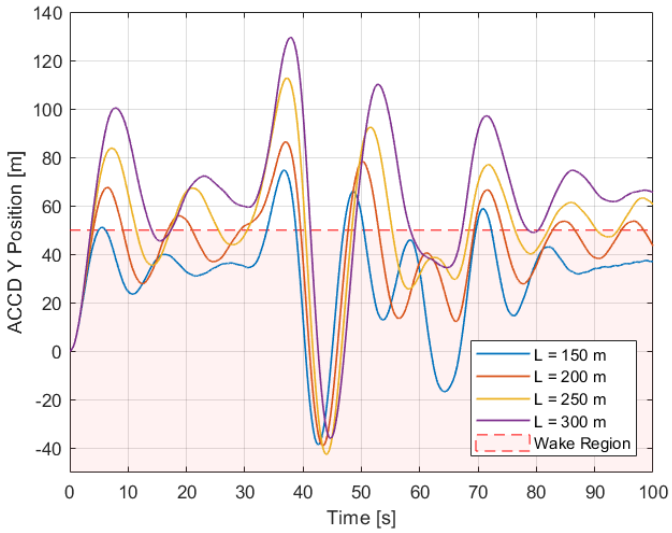

Figure 4.25: ACCD vertical position with control inputs, aircraft wake enabled.

Figure 4.26 compares the final vertical position with and without the wake model, for a 300m long rope. The wake leads to larger swings when the ACCD crosses that region, but overall it remains manageable. Generally, critical issues associated with wake are not found. Nonetheless, it's crucial to prevent a scenario akin to the one illustrated in Figure 4.24. Consequently, opting for a longer 300-meter rope is favored.

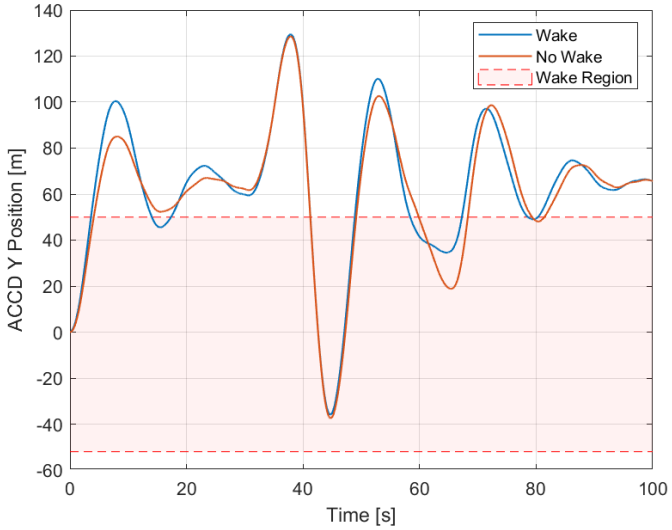

Figure 4.26: ACCD vertical position with and without aircraft wake.

5 Conclusion and Future Work

This work aimed at developing an accurate and computationally efficient model for the simulation of the rope dynamics. To achieve this, a novel Multibody approach was introduced, providing a flexible framework to incorporate all the necessary features. The model has been tested in a number of test cases, before being applied to the larger scale IAC simulation. Based on the mission requirements, suitable rope specifications are proposed. In this chapter, the simulation results are discussed, addressing the research questions formulated in the Introduction. The discussion also includes an examination of the limitations of the present model, along with recommendations for further research and improvements.

5.1 Conclusions

In general, the presented model constitutes a versatile framework flexible to customization for specific application requisites. Several features have been proposed to address the requirements inherent to the context of the IAC maneuver. The rope model has been first tested in simpler test cases, to verify its reasonableness. When inserted into the larger scale IAC simulation, it allowed to propose a suitable set of specifications for the rope model.
Conclusions will be drawn based on the research questions that were formulated in the Introduction of the present work.

- *Does the model provide a sufficiently accurate representation of the physics governing the rope dynamics? Can it effectively describe the oscillations commonly observed in slender bodies?*

  Rope bodies exhibit intricate and nonlinear dynamics, due to their capacity for accommodating substantial deflection and deformation. Validation of the presented model necessitates a comparative analysis against empirical data. Given the absence of publicly available benchmarks in the literature, the aim of the current work is focused solely on the verification of the model and its associated features. An analysis of energy conservation was undertaken across various test scenarios. The model seems to provide a valid description of the underlying physics. Throughout the test instances, the rope demonstrates a behavior which agrees with the intuition, as discerned from an examination of its kinematic characteristics.

- *What are appropriate rope material and specifications for the IAC mission?*

  It was observed that steel wire ropes of such lengths possess excessive mass. This substantial inertia characteristic poses implications for the stability properties of the ACCD, resulting in extended oscillatory behaviors near the equilibrium state. In contrast, UHMWPE ropes offer a more expeditious and stable repositioning of the ACCD, while concurrently maintaining or even surpassing stress failure thresholds. A diameter of 0.024 m emerges as to be suitable to handle the most stressful configuration, with commendable factor of safety. While the potential

inclusion of larger diameters may exert a modest influence on stability characteristics, the resultant impact is deemed of minor consequence. Furthermore, ropes with larger diameters manifest lower settling positions, thereby attenuating potential perturbations arising from wake phenomena.

Longer ropes grant the ACCD greater freedom of movement in space. Modest control inputs to the capturing device flaps detection yield large repositioning. Nonetheless, this gives rise to larger overshoots and oscillation periods, which must be limited. Faster displacements can potentially allow for more capturing attempts in the same formation flight. In the end, longer ropes remain the more favorable choice as they steer clear of the aircraft wake area, preventing its destabilizing impact on the system's control. Optimal compromise in this regard appears to be a 300 m rope length. However, in future control simulations, it must be checked if longer settling times can compromise the capability of performing multiple maneuvers with the limited formation time.

- *Is the capturing system stable in the reference configuration? Does the wake of the aircraft affect the maneuverability of the system?*

  The capturing system generally achieves aerodynamic stability, predominantly attributed to the ACCD properties. Utilizing UHMWPE as the rope material has enabled the preservation of these characteristics, owing to its low weight and inertia. The ACCD demonstrates remarkable maneuverability when flap deflections are executed through control inputs. Even after repositioning, the capturing system will settle into a stable, steady-state arrangement. The aircraft's wake generates an area where the airflow velocities could be altered, potentially introducing chaotic effects. This becomes critical for ropes ranging from 200 to 250 meters in length, as they tend to settle near the edge of the wake zone. During the process of converging to a stable position, oscillations intensify due to the continuous entry and exit from the wake region. As previously discussed, a longer rope of 300 meters largely avoids the wake region. If control inputs cause the ACCD to move within the wake zone, this might slightly increase the oscillation overshoot. Nonetheless, the reference configuration remains stable.

- *Does the final set of ODEs manifest numerical problems during the integration? Is it sensitive to the type of ODE solver used and the choice of the integration step size?*

  Stiffness phenomena have been observed in the integration of the equations of motion, particularly evident when employing a fine mesh in conjunction with elevated damping coefficients. Implicit ODE solvers are recognized as optimal for addressing such challenges. This assertion is confirmed by simulation outcomes: employing the BDF2 integration scheme ensures stable simulations across all tested setups. Nonetheless, given their computational load, explicit schemes are preferred. Higher-order RK solvers mitigate some of the instability concerns, rendering them suitable for reasonably demanding scenarios.

- *Is it possible to achieve a reasonable trade-off between accuracy and computation time?*

  A fine mesh for the rope is not needed in the IAC simulation. As previously discussed, when significant forces are exerted on the rope, the body will mostly assume a straight configuration, eliminating the need to account for substantial deformations and displacements. In the simulations, noticeable discrepancies in outcomes are indiscernible when employing more than 20 elements to represent the rope. Consequently, adopting this value for the discretization parameter is a suitable balance between computational efficiency and accuracy. Interestingly, in situations where the RLV is connected and subject to very large loads, it could even be sensible to transition to a simplified beam model. This arises due to the magnitudes of the forces involved. Regarding integration strategies, explicit methods should be favored if they demonstrate stability at the chosen step size. Fourth and eighth-order Runge-Kutta methods typically maintain integration stability across a majority of hyperparameter configurations. The parallelization of the software across multiple cores has facilitated faster computations without imposing constraints on other processes.

5.2 Limitations and Future Work

In this final section, the limitations of the current study are addressed, proposing recommendations to shape the trajectory of future research. Initially, we will examine the constraints associated with the modelling methodology. Subsequently, we will discuss the next scenarios of the IAC maneuver that shall be simulated. Lastly, we will delve into strategies aimed at further accelerating computations and solving the numerical challenges.

Modelling Methodology:

In its current developmental phase, the suggested model does not take into account torsional or twisting effects for the rope. Presently, the connection between the lower end of the rope and the ACCD can be perceived as an ideal, frictionless revolute joint, enabling rotation around the roll axis. It is expected that the ropes' torsional stiffness is not significant, especially for the lengths proposed within our application. Indeed, as the rope length increases, its torsional stiffness decreases. Ropes of this particular length can undergo multiple rotations around their central axis without incurring significant reactive torque. This aspect could potentially impact the rope's breaking strength, if an unstable configuration is reached. Moreover, even if modest, the torsional stiffness of the rope might aid in stabilizing the ACCD roll rotations. The outlined MBS is a relatively adaptable framework. It is possible to introduce a set of angles to describe torsional displacement which, depending on the formulation, could potentially be interconnected with other variables.

Furthermore, as discussed in Section 3.3.1, the current modelling of the bending stiffness simplifies the 3D description of the rope. In fact, two bending moments are introduced, describing the deflection of the body in the x-y and x-z planes. In this

way, it was possible to simplify the expression of the rope curvature, from a complex formula for the 3D case to an easier one which describes a 2D curve. Nevertheless, this method de facto decouples the angular coordinates, handling them separately in their respective planes. While the approach provides reasonably accurate results, it is not a rigorous description of the underlying physics. Therefore, future work shall examine if applying the 3D curvature description improves the model accuracy significantly.

As widely discussed, a complete validation of the model necessitates a comparative analysis with empirical data. While the fundamental depiction of the physics has undergone verification via the analysis of the energy balance, features like the body's frequency response are yet to be validated. This aspect is especially critical, due to the unavailability of direct damping coefficient data in material specifications. This mode of validation remains indispensable for any model proposed for this application, including those which can be tested through the beam benchmark. In fact, satisfying the beam theory does not inherently ensure precision in scenarios involving large displacement and deformation.

Generally, retaining a more precise implementation based on the finite element method would serve as a valuable reference for comparison. Although this approach is likely to be inherently slower, regardless of the techniques employed for implementation or parallelization, the resulting accuracy is likely to be considerably enhanced. Only after this step can a genuine trade-off be comprehensively assessed. The ANCF approach has convincingly proven its suitability for addressing the challenges posed by large displacements and deformations. Continuing to advance in this direction holds substantial promise: an intricate engineering feat such as the IAC maneuver necessitates meticulousness in evaluating rope stresses and kinematics. Nevertheless, the model proposed in this work still offers a computationally light tool that adeptly addresses the requirements, facilitating the estimation of numerous parameters within the expanded simulation.

Future IAC Simulations:

In the present work, the simulations were conducted assuming a cruise flight configuration for the towing aircraft. In subsequent stages of the IAC mission validation, it will become imperative to replicate the deployment sequence of the capturing system. This sequence involves the gradual release of the rope and capturing device from the aircraft, and it may introduce unique forces and torques that could pose potential challenges. A not fully deployed rope is lighter. Consequently, it can get closer to the wake region, potentially compromising the instability of the system. In the proposed model, the rope's length is integrated into the equations of motion as a hyperparameter. Therefore, simulating the deployment could be relatively straightforward if the rope length is incrementally extended. If this process is performed slowly enough, the angles used to define the rope's state will naturally adapt to represent the new length.

The model also needs to be tested during the TA gliding phase. This step is characterized by the towing aircraft's descent without propulsion, intended to synchronize with the RLV's motion. In such a scenario, the relative airflow's direction will alter, leading to corresponding shifts in drag and lift forces. Consequently,

the capturing system will adopt a new stable position, likely higher in its vertical alignment. This adjustment could potentially trigger stability concerns, as segments of the rope might intersect the region where the aircraft's wake exerts maximum influence. It might be necessary to propose new rope length values in order to attain a configuration of heightened stability. This specific configuration is paramount for executing the capturing phase. Given that the responsiveness to control inputs is a pivotal requirement, a comprehensive new analysis is imperative from this perspective.

Computational Efficiency and Numerical Stability:

As extensively discussed in the Section 4, the rope needs a detailed mesh only in specific cases to get accurate results. In fact, the higher the forces in play, the more the rope approaches a configuration where it's completely straight. In these cases, there is no need for a high describing power to catch both low and high frequency oscillations, because everything will dampen out and leave space to just the longitudinal deformation. Therefore, we might want to consider the use of an adaptive mesh, depending on the stresses and the configuration. On the other hand, modifying the number of elements employed in the discretization of the rope might present more intricate issues. This is because interpolation of the values of the rope angles would be necessary to attribute meaningful states to the new mesh configuration.

Lastly, additional efforts can be directed towards improving the handling of numerical challenges that arise during the integration steps. In this work, a sensitivity analysis on the rope model parameters was performed, and it showed that the ODEs manifest the stiffness phenomena for some configurations of the parameters. Implicit solvers have shown to remain stable in all cases, while explicit ones struggle to be stable with the required step size. However, the first have a much larger computational overhead, because they require the solution of an equation at every time step, and the call to the ODE function is expensive. Therefore, it is advisable to perform future work aimed at implementing an implicitly-based scheme in the integration of the equations of motion.

References

[1] Harry W Jones. The recent large reduction in space launch cost. *48th International Conference on Environmental Systems*, 2018.

[2] Sunayna Singh, Martin Sippel, and Sven Stappert. Full-scale simulation and analysis of formation flight during in-air-capturing of a winged reusable launch vehicle. *Journal of Space Safety Engineering*, 9, 2022.

[3] Davide Sivolella. *The Space Shuttle Program*. Springer Cham, 2017.

[4] Antoine Patureau de Mirand, Jean Marc Bahu, and Olivier Gogdet. Ariane next, a vision for the next generation of ariane launchers. *Acta Astronautica*, 170, 2020.

[5] Martin Sippel, Sven Stappert, Leonid Bussler, Stefan Krause, Sebastian Cain, Javier Espuch, and Sophia Buckingham. Highly efficient rlv-return mode "in-air-capturing" progressing by preparation of subscale flight tests. *8th European Conference For Aeronautics And Space Sciences (EUCASS)*, 2019.

[6] Sunayna Singh, Sven Stappert, Sophia Buckingham, Silvania Lopes, Yakut Cansev, Madalin Simioana, Mihai Pripasu, Andreas Wiegand, Martin Sippel, and Philippe Planquart. Dynamic modelling and control of an aerodynamically controlled capturing device for 'in-air- capturing' of a reusable launch vehicle. *11th International ESA Conference on Guidance, Navigation & Control System (GNC)*, 2021.

[7] Sunayna Singh, Madalin Simioana, Sven Stappert, Martin Sippel, and Yakut Kucukosman. Control design and analysis of a capturing device performing in-air capturing of a reusable launch vehicle. *9th European Conference For Aeronautics And Space Sciences (EUCASS)*, 2022.

[8] Zhen Li, Julian Erskine, Stéphane Caro, and Abdelhamid Chriette. Design and control of a variable aerial cable towed system. *IEEE Robotics and Automation Letters*, 5, 2020.

[9] Z.H. Zhu and S.A. Meguid. Modeling and simulation of aerial refueling by finite element method. *International Journal of Solids and Structures*, 44, 2007.

[10] Haitao Wang, Xinmin Dong, Jianping Xue, and Jiaolong Liu. Dynamic modeling of a hose-drogue aerial refueling system and integral sliding mode backstepping control for the hose whipping phenomenon. *Chinese Journal of Aeronautics*, 27, 2014.

[11] Omega. Aerial refueling services, 2023. https://www.omegaairrefueling.com/our-fleet/, [Acccessed: 01 June 2023].

[12] University of Michigan. Space tethers, 2015. https://ece.engin.umich.edu/stories/space-tethers-can-be-used-to-fling-spacecraft-into-interplanetary-space, [Acccessed: 01 June 2023].

[13] Leo Chen, Rui Huang, Liping He, Xianlin Ren, and Bin Zheng. Dynamical modelling and control of space tethers: a review of space tether research. *Nonlinear Dynamics*, 77, 2014.

[14] Bradley C. Edwards. Design and deployment of a space elevator. *Acta Astronautica*, 47, 2000.

[15] Shihao Luo, Naigang Cui, Xiaowei Wang, Youhua Fan, and Run Shi. Model and optimization of the tether for a segmented space elevator. *Aerospace*, 9, 2022.

[16] Ellis Harold Dill. Kirchhoff's theory of rods. *Archive for History of Exact Sciences*, 44, 1992.

[17] Beta Lam, Frederick Li, Jianmin Zhao, Rynson Lau, and Taku Komura. Efficient modelling of flexible connectors. In *2008 First IEEE International Conference on Ubi-Media Computing*, 2008.

[18] Naijing Lv, Jianhua Liu, Xiaoyu Ding, Jiashun Liu, Haili Lin, and Jiangtao Ma. Physically based real-time interactive assembly simulation of cable harness. *Journal of Manufacturing Systems*, 43, 2017. Special Issue on the 12th International Conference on Frontiers of Design and Manufacturing.

[19] Tsung-Chih Tsai. *Position Based Dynamics*, pages 1–5. Springer International Publishing, Cham, 2017.

[20] Arkadiusz Żak and Wiktor Waszkowiak. A spline-based fe approach to modelling of high frequency dynamics of 1-d structures. *Computers & Mathematics with Applications*, 104, 2021.

[21] Ahmed A. Shabana. Flexible multibody dynamics: Review of past and recent developments. *Multibody System Dynamics*, 1997.

[22] A A Nada, B A Hussein, S M Megahed, and A A Shabana. Use of the floating frame of reference formulation in large deformation analysis: Experimental and numerical validation. *Proceedings of the Institution of Mechanical Engineers, Part K: Journal of Multi-body Dynamics*, 224, 2010.

[23] Naijing Lv, Jianhua Liu, Huanxiong Xia, Jiangtao Ma, and Xiaodong Yang. A review of techniques for modeling flexible cables. *Computer-Aided Design*, 2020.

[24] Oliver M. O'Reilly. *Kirchhoff's Rod Theory*. Springer International Publishing, Cham, 2017.

[25] M. B. Rubin. *Cosserat Theories: Shells, Rods and Points*. Springer Dordrecht, 2000.

[26] Refaat Yakoub and Ahmed Shabana. Three dimensional absolute nodal coordinate formulation for beam elements: Implementation and applications. *Journal of Mechanical Design*, 2001.

[27] Ahmed Shabana. An overview of the ancf approach, justifications for its use, implementation issues, and future research directions. *Multibody System Dynamics*, 58, 2023.

[28] P.J. Davis and P. Rabinowitz. *Methods of Numerical Integration*. Dover Books on Mathematics Series. Dover Publications, 2007.

[29] Kapseong Ro and James Kamman. Modeling and simulation of hose-paradrogue aerial refueling systems. *Journal of Guidance Control and Dynamics*, 33:53–63, 2010.

[30] Paweł Fritzkowski and Henryk Kaminski. Dynamics of a rope as a rigid multibody system. *Journal of Mechanics of Materials and Structures*, 3, 2008.

[31] Paweł Fritzkowski and Henryk Kamiński. Dynamics of a rope modeled as a discrete system with extensible members. *Computational Mechanics*, 44, 2009.

[32] Paweł Fritzkowski and Henryk Kamiński. Dynamics of a rope modeled as a multi-body system with elastic joints. *Computational Mechanics*, 46, 2010.

[33] Pawel Fritzkowski and Henryk Kaminski. A discrete model of a rope with bending stiffness or viscous damping. *Acta Mechanica Sinica/Lixue Xuebao*, 27, 2011.

[34] G.A. Korn and T.M. Korn. *Mathematical Handbook for Scientists and Engineers: Definitions, Theorems, and Formulas for Reference and Review*. Dover Civil and Mechanical Engineering. Dover Publications, 2013.

[35] Herbert Goldstein. *Classical Mechanics*. Addison-Wesley, 1980.

[36] M. Kline. *Calculus: An Intuitive and Physical Approach*. Dover Books on Mathematics. Dover Publications, 1998.

[37] R.W. Fitzgerald. *Mechanics of Materials*. Addison-Wesley Publishing Company, 1982.

[38] A.P. French. *Newtonian Mechanics*. M.I.T. introductory physics series. W.W. Norton, 1971.

[39] Ji Hoon Lee, Ludvig Karlsen, and Chun Woo Lee. A method for improving the dynamic simulation efficiency of underwater flexible structures by implementing non-active points in modelling. *ICES Journal of Marine Science*, 65(9), 2008.

[40] John D. Anderson. *Fundamentals of aerodynamics*. McGraw-Hill, 5th edition, February 2011.

[41] E. Hairer, S.P. Nørsett, and G. Wanner. *Solving Ordinary Differential Equations II: Stiff and Differential-Algebraic Problems*. Solving Ordinary Differential Equations II: Stiff and Differential-algebraic Problems. Springer, 1993.

[42] Maplesoft, a division of Waterloo Maple Inc.. Maple, 2021.

[43] Siu Kwan Lam, Antoine Pitrou, and Stanley Seibert. Numba: A LLVM-based Python JIT compiler, 2015.

[44] Inc. The Mathworks. MATLAB version 9.14.0.2306882 (2023a), 2023.

[45] Ethan Lockwood. Book of curves. 1963.

[46] Sunayna Singh, Leonid Bussler, Steffen Callsen, Sven Stappert, Silvania Lopes, and Sophia Buckingham. A superposition approach to aerodynamic modelling of a capturing device used for in-air capturing of a reusable launch vehicle. In *9th European Conference For Aeronautics And Space Science, EUCASS 2022*, June 2022.

[47] G. Norris and M. Wagner. *Airbus A340 and A330*. Jetliner history. MBI, 2001.

[48] Martin Sippel, Sven Stappert, and Madalin Simioana. Technical report on different rlv return modes' performances, 2020.

[49] Teufelberger. Hyperten, technical fiber rope, 2023. https://www.teufelberger.com/en/hyperten-technical-fiber-rope.html, [Acccessed: 01 June 2023].

[50] The Engineering Toolbox. Wire rope strength, 2023. https://www.engineeringtoolbox.com/wire-rope-strength-d_1518.html, [Acccessed: 01 June 2023].

A Full Equations of Motion

The final equations of motion, before the transformation to a first-order system, can be schematized as follows:

$$\boldsymbol{M}(\boldsymbol{q})\ddot{\boldsymbol{q}} = \boldsymbol{f}(t, \boldsymbol{q}, \dot{\boldsymbol{q}})$$

where:

$$\boldsymbol{M}(\boldsymbol{q}) = \begin{bmatrix} M_{1,1} & M_{1,2} & \cdots & M_{1,k} \\ M_{2,1} & M_{2,2} & \cdots & M_{2,k} \\ \vdots & \vdots & \ddots & \vdots \\ M_{k,1} & M_{k,2} & \cdots & M_{k,k} \end{bmatrix}, \quad \boldsymbol{f} = \begin{bmatrix} f_1 \\ f_2 \\ \vdots \\ f_k \end{bmatrix},$$

k is the total number of variables in the system, and is equal to $2n + 1$. In fact, two angle variables per element (ϕ_i and ψ_i) and the elongation variable s are used in the final system.

The set of equations is rather complex because of the interaction of the two set of angles, and the complicated expression of the inertia forces that appear in the right-hand side. In addition to this, the elongation variable at the beginning adds an extra layer of complexity. A much cleaner expression for the equations of motion could be obtained without the introduction of s.

A.1 Mass Matrix

The in-depth scheme of the mass matrix $\boldsymbol{M}$ is hereby presented. The matrix is symmetric, so the lower triangular part has been omitted. The entries have been ordered such that they follow the order of the variables: $[s, \phi_1, ..., \phi_n, \psi_1, ..., \psi_n]$. For readability purposes, the matrix is divided in sub-blocks:

$$\boldsymbol{M}(\boldsymbol{q}) = \begin{bmatrix} nmL & M_{s\phi_1} & \cdots & M_{s\phi_n} & M_{s\psi_1} & \cdots & M_{s\psi_n} \\ & M_{\phi_{1,1}} & \cdots & M_{\phi_{1,n}} & M_{\phi\psi_{1,1}} & \cdots & M_{\phi\psi_{1,n}} \\ & & \ddots & \vdots & \vdots & \ddots & \vdots \\ & & & M_{\phi_{n,n}} & M_{\phi\psi_{n,1}} & \cdots & M_{\phi\psi_{n,n}} \\ & & & & M_{\psi_{1,1}} & \cdots & M_{\psi_{1,n}} \\ & & & & & \ddots & \vdots \\ & & & & & & M_{\psi_{n,n}} \end{bmatrix}$$

Using the same notation used above, we can specify the expression for the matrix entries:

$$M_{s\phi_j} = -b_j mL \cos\psi_1 \cos\psi_j \sin\left(\phi_j - \phi_1\right)$$

$$M_{s\psi_j} = b_j mL \left[\cos\psi_j \sin\psi_1 - \cos\psi_1 \sin\psi_j \cos\left(\phi_j - \phi_1\right) \right]$$

$$M_{\phi_{i,j}} = \begin{cases} m\cos\left(\psi_1\right)^2 \left(c_i L^2 + 2b_i sL + ns^2\right) + \dfrac{L^2}{12} & \text{for } i = j, j = 1 \\ \dfrac{mL^2}{12}\left(c_i \cos\left(\psi_i\right)^2 + 1\right) & \text{for } i = j, j \neq 1 \\ b_j\, h_i\, mL \cos\psi_i \cos\psi_j \cos\left(\phi_j - \phi_i\right) & \text{else} \end{cases}$$

$$M_{\phi\psi_{i,j}} = -b_j mL\, h_i \cos\psi_i \sin\psi_j \sin\left(\phi_j - \phi_i\right)$$

$$M_{\psi_{i,j}} = \begin{cases} b_{i,j}\, mL^2 + 2b_i msL + nms^2 & \text{for } i = 1, j = 1 \\ b_{i,j}\, h_i\, mL \left[\cos\psi_i \cos\psi_j + \sin\psi_i \sin\psi_j \cos\left(\phi_j - \phi_i\right) \right] & \text{else} \end{cases}$$

The following parameters were used to lighten the notation:

$$h_i = \begin{cases} L + s & \text{for } i = 1 \\ L & \text{else} \end{cases}$$

$$b_i = \frac{2(n-i)+1}{2}$$

$$c_i = \frac{3(n-i)+1}{3}$$

$$d_i = \frac{4(n-i)+1}{4}$$

A.2 Right-Hand-Side

Right-hand side assumes a convoluted expression, due to the complex expression of inertia forces. The overall structure is the following:

$$rhs = \begin{bmatrix} f_s \\ f_{\phi_1} \\ f_{\phi_2} \\ \vdots \\ f_{\phi_n} \\ f_{\psi_1} \\ f_{\psi_2} \\ \vdots \\ f_{\psi_n} \end{bmatrix}$$

The elongation variable s also affects the expression for the first azimuth angle. As a matter of fact, it is necessary to separately describe the elements f_{ϕ_1} and the remaining components $f_{\phi_2}, ..., f_{\phi_n}$. The same reasoning applies to the side-slip angle components.

$$
\begin{aligned}
f_s = \quad & mL\cos\psi_1 \sum_{j=2}^{n} b_j \cos\psi_j \cos\left(\phi_j - \phi_1\right)\left(\dot{\phi_j}^2 + \dot{\psi_j}^2\right) \\
& -2mL\cos\psi_1 \sum_{j=2}^{n} b_j \sin\psi_j \sin\left(\phi_j - \phi_1\right)\dot{\phi_j}\dot{\psi_j} \\
& +\frac{mL}{2}\sin\psi_1 \sum_{j=2}^{n} b_j \sin\psi_j \dot{\psi_j}^2 \\
& +\left(b_1 mL + nms\right)\left[\dot{\phi_1}^2 \left(\cos\psi_1\right)^2 + \dot{\psi_1}^2\right]
\end{aligned}
$$

$$
\begin{aligned}
f_{\phi_1} = \quad & mL\, h_1 \cos\psi_1 \sum_{j=2}^{n} b_j \cos\psi_j \sin\left(\phi_j - \phi_1\right)\left(\dot{\phi_j}^2 + \dot{\psi_j}^2\right) \\
& +2mL\, h_1 \cos\psi_1 \sum_{j=2}^{n} b_j \sin\psi_j \cos\left(\phi_j - \phi_1\right)\dot{\phi_j}\dot{\psi_j} \\
& +2m\cos\psi_1 \sin\psi_1 \left(c_1 L^2 + 2b_1 sL + ns^2\right)\dot{\phi_1}\dot{\psi_1} \\
& -2m\left(\cos\psi_1\right)^2 \left(b_1 L + ns\right)\dot{s}\,\dot{\phi_1}
\end{aligned}
$$

$$
\begin{aligned}
f_{\phi_i} = \quad & mL\cos\psi_i \sum_{j=2}^{n} h_j\, b_j \cos\psi_j \sin\left(\phi_j - \phi_i\right)\left(\dot{\phi_j}^2 + \dot{\psi_j}^2\right) \\
& +2mL\cos\psi_i \sum_{j=2}^{n} h_j\, b_j \sin\psi_j \cos\left(\phi_j - \phi_i\right)\dot{\phi_j}\dot{\psi_j} \\
& +2b_i\, mL\cos\psi_i\, \dot{s}\left[\sin\psi_1 \sin\left(\phi_i - \phi_1\right)\dot{\psi_1} - \cos\psi_1 \cos\left(\phi_i - \phi_1\right)\dot{\phi_1}\right] \\
& +2c_i mL^2 \cos\psi_i \sin\psi_i\, \dot{\phi_i}\dot{\psi_i}
\end{aligned}
$$

$$
\begin{aligned}
f_{\psi_1} = \quad & -mL\, h_1 \sin\psi_1 \sum_{j=2}^{n} b_j \cos\psi_j \cos\left(\phi_j - \phi_1\right)\left(\dot{\phi_j}^2 + \dot{\psi_j}^2\right) \\
& +2mL\, h_1 \sin\psi_1 \sum_{j=2}^{n} b_j \sin\psi_j \sin\left(\phi_j - \phi_1\right)\dot{\phi_j}\dot{\psi_j} \\
& +mL\, h_1 \cos\psi_1 \sum_{j=2}^{n} b_j \sin\psi_j \dot{\psi_j}^2 \\
& -m\cos\psi_1 \sin\psi_1\, \dot{\phi_1}^2 \left(c_1 L^2 + 2b_1 sL + ns^2\right) \\
& -2m\left(b_1 L + ns\right)\dot{s}\,\dot{\psi_1}
\end{aligned}
$$

$$
\begin{aligned}
f_{\psi_i} = \quad & -mL \sin\psi_i \sum_{j=2}^{n} h_j\, b_j \cos\psi_j \cos\left(\phi_j - \phi_i\right) \left(\dot{\phi_j}^2 + \dot{\psi_j}^2\right) \\
& +2mL \sin\psi_i \sum_{j=2}^{n} h_j\, b_j \sin\psi_j \sin\left(\phi_j - \phi_i\right) \dot{\phi_j}\dot{\psi_j} \\
& +mL \cos\psi_i \sum_{j=2}^{n} b_j\, h_1 \sin\psi_j\, \dot{\psi_j}^2 \\
& +2b_i\, mL \sin\psi_i\, \dot{s} \left[\cos\psi_1 \sin\left(\phi_i - \phi_1\right) \dot{\phi_1} - \sin\psi_1 \cos\left(\phi_i - \phi_1\right) \dot{\psi_1}\right] \\
& -2b_i\, mL \cos\psi_1 \cos\psi_i\, \dot{s}\, \dot{\psi_1} \\
& -c_i mL^2 \cos\psi_i \sin\psi_i\, \dot{\phi_j}^2
\end{aligned}
$$

Gravity has been omitted from the equations, since it can be modelled as a distributed external force. The final right-hand side for the system, adding the contribution of the non-lagrangian components, will be:

$$
\boldsymbol{rhs} = \boldsymbol{f} + \boldsymbol{Q}_D + \boldsymbol{Q}_M + \boldsymbol{Q}_{aero} + \boldsymbol{Q}_{ext} \tag{A1}
$$

where $\boldsymbol{Q}_D$, $\boldsymbol{Q}_M$, $\boldsymbol{Q}_{aero}$ and $\boldsymbol{Q}_{ext}$ are described in Section 3.

The IAC simulation required the addition of a lumped mass at the end of the rope, to simulate the presence of the ACCD. This can be done by modifying all entries of the mass matrix and right-hand side. The correction term is exactly the same as the equations aforelisted, but using the lumped mass instead of the mass of the rope element. In the calculation of this new term, the parameters b_i, c_i, d_i and n must not be considered.